colloids and interfaces

MDPI

Article

Bentonite Nanoparticle Stability and the Effect of Fulvic Acids: Experiments and Modelling

Holger Seher [1,*], Horst Geckeis [2], Thomas Fanghänel [3,4] and Thorsten Schäfer [5]

1 Gesellschaft für Anlagen und Reaktorsicherheit (GRS) gGmbH, Schwertnergasse 1, 50667 Köln, Germany
2 Karlsruhe Institute of Technology, Institute for Nuclear Waste Disposal (INE), P.O. Box 3640, 76021 Karlsruhe, Germany; horst.geckeis@kit.edu
3 European Commission, Joint Research Centre, Institute for Transuranium Elements, 76021 Karlsruhe, Germany; Thomas.Fanghaenel@ec.europa.eu
4 Ruprecht-Karls-Universität Heidelberg, Institute of Physical Chemistry, Im Neuenheimer Feld 253, 69120 Heidelberg, Germany
5 Friedrich-Schiller-Universität Jena, Institute for Geosciences (IGW), Applied Geology, Burgweg 11, 07749 Jena, Germany; thorsten.schaefer@uni-jena.de
* Correspondence: holger.seher@grs.de

Received: 24 March 2020; Accepted: 16 April 2020; Published: 21 April 2020

Abstract: In this study, the critical coagulation concentration (CCC) for FEBEX bentonite colloids is determined by colloid coagulation studies under variation of pH, electrolyte concentration, and fulvic acid (GoHy-573FA) content. For $CaCl_2$ electrolyte solution, a pH-independent Ca-CCC of 1 mmol L^{-1} is found. In the case of NaCl background electrolyte, a pH-dependent Na-CCC can be determined with 15 ± 5 mmol L^{-1} at pH 6, 20 ± 5 mmol L^{-1} at pH 7, 200 ± 50 mmol L^{-1} at pH 8, 250 ± 50 mmol L^{-1} at pH 9, and 350 ± 100 mmol L^{-1} at pH 10, respectively. The addition of 1 mg L^{-1} dissolved organic carbon in the form of fulvic acid (FA) increases the Ca-CCC to 2 mmol L^{-1}. An association of FA with FEBEX bentonite colloids as surface coating can clearly be identified by scanning transmission X-ray microscopy (STXM). The experimental bentonite stability results are described by means of an extended DLVO (Derjaguin–Landau–Verwey–Overbeek) approach summing up hydration forces, short-range Born repulsion, van der Waals attraction, and electrical double layer repulsion. The measured zeta (ζ)-potential of the bentonite colloids is applied as platelet face electrokinetic potential and the edge electrokinetic potential is estimated by the combination of silica and alumina ζ-potential data in the ratio given by the FEBEX bentonite structural formula. Adjusting the montmorillonite face electrokinetic potential by a maximum of ±15.9 mV is sufficient to successfully reproduce the measured stability ratios. Due to the uncertainty in the ζ-potential measurement, only semiquantitative calculations of the stability ratio can be given.

Keywords: colloid stability; CCC; FEBEX bentonite; DLVO; zeta potential

1. Introduction

In many concepts for deep geological disposal of high-level nuclear waste in crystalline host rocks, the waste is emplaced inside a metal canister surrounded by a bentonite buffer [1,2]. The bentonite acts, inter alia, as a hydrogeological barrier delaying the contact of the canister with formation water and retarding the radionuclide release to the geosphere by means of its high sorption capacity and a diffusion-controlled transport. After contact with water from a water-conducting feature (e.g., a fracture), the bentonite buffer material will swell to some extent into these fractures due to its high swelling capacity [3]. Bentonite colloids may detach from the formed gel layer [4–7] and thus be a source of mobile colloidal phases potentially acting as a carrier for strongly sorbing radionuclides [8].

Transport of man-made as well as naturally occurring radionuclides by colloids has been reported, e.g., for the Nevada Test Site, USA [9,10] and the Whiteshell Research Area, Canada [11]. In the colloid and radionuclide retardation (CRR) experiment performed at the Grimsel Test Site (GTS, Switzerland; Phase V), colloid-mediated transport of trivalent and tetravalent radionuclides (Am(III), Pu(IV), Th(IV)) was found to be occurring in the migration (MI) shear zone under the given hydraulic conditions [12,13]. In the successive colloid formation and migration experiment (CFM), huge geotechnical effort was undertaken to hydraulically isolate the MI shear zone from the artificial hydraulic gradient due to the GTS tunnel construction. After several conservative and "homologue" tracer tests, radioactive tracer tests were performed [14–16].

A prerequisite for colloid migration is the stability of colloids against agglomeration/aggregation in solution. Colloids might aggregate and consequently face high filter factors limiting their mobility. Therefore, the colloid stability is a key parameter for colloid-facilitated transport. It is determined by means of the stability ratio W, which is defined as the fastest coagulation rate r_{fast} of single colloid to doublet formation in the system of interest (purely diffusion-controlled aggregation) to the actual coagulation rate of doublet formation r_{actual} [17,18]. A stability ratio is colloid-size-independent [19]. The critical coagulation concentration (CCC) refers to the $[Me^{+}]$ or $[Me^{2+}]$ concentration at the transition of fast, purely diffusion-controlled to slow coagulation. This transition is also observed for the stability ratio where W transitions from higher values to 1. The dynamic light scattering technique (photon correlation spectroscopy; PCS) is frequently used to determine the coagulation rate and CCC of various clay colloid suspensions [17,18,20–22].

One of the many bentonites investigated in waste repository projects is the bentonite used in the full-scale high-level waste engineering barrier experiment (FEBEX) at the GTS [23,24]. A montmorillonite platelet, the major colloidal phase found to be mobilised from FEBEX bentonite [4,6], consists of individual or several layers stacked together, with each individual layer built of an octahedral sheet sandwiched into two tetrahedral sheets. The face of a montmorillonite platelet has a pH-independent permanent negative electrokinetic potential due to the isomorphous substitution of Si^{4+} by lower valent cations (e.g., Al^{3+}) in the tetrahedral, or in the case of Al^{3+} substitution by Mg^{2+} or Fe^{2+}, in the octahedral sheet [25]. The montmorillonite edges consist of broken tetrahedral and octahedral sheets exposing silanol and aluminol groups that represent a pH-dependent edge electrokinetic potential. At low pH values, the edge surfaces are protonated due to an excess of protons and are deprotonated/hydroxylated with increasing pH value [26–28]. Due to the morphology of the platelet, three different modes of interaction can be distinguished: edge–face (EF), edge–edge (EE), and face–face (FF).

The sum of the face electrokinetic potential and the edge electrokinetic potential result in an overall layer electrokinetic potential which influences the rheological parameters (e.g., plastic viscosity or yield stress) of a clay or clay colloids due to the resulting electrostatic components of interaction. Other factors such as electrolyte ionic strength and pH, tetrahedral layer electrokinetic potential, other fine-grained minerals, and the particle size and shape have an impact, too [29]. Sun et al. [30] described a decrease in the swelling capacity of montmorillonites with increasing tetrahedral layer electrokinetic potential. With higher tetrahedral layer electrokinetic potential, the released colloids for Na-clays increase in colloid size and released colloid mass [31].

For montmorillonite colloid stability analyses, the isoelectric point (pH_{iep}), corresponding to the zeta (ζ)-potential-determined charge neutrality of the pH-dependent platelet edges, is of great importance. For pH values lower than the pH_{iep}, an attractive edge–face interaction due to the attraction of negative platelet face electrokinetic potentials and positive platelet edge electrokinetic potentials leads to aggregates of "card-house"-type structures [26]. Above the pH_{iep}, both the edge and face of the platelet have a negative electrokinetic potential leading to higher colloid stability.

In order to be able to predict montmorillonite colloid stability by an extended DLVO theory (Derjaguin–Landau–Verwey–Overbeek) [32,33], the overall surface potential has to be separated into potentials and interaction modes associated with the edge and face geometry of the montmorillonite

platelets. The classical DLVO theory would oversimplify the montmorillonite geometry because it employs a sphere or plate model with one surface potential. The geometrical assumption adapted from Mahmood et al. [34] to calculate the total interaction energy is to use a half cylinder with the radius equal to half the thickness of the platelet. Interaction between a flat face and a half cylinder is adapted using the Derjaguin interaction procedure [35]. The total interaction energy was calculated by summing up DLVO interaction energy (Born repulsion, electric double layer repulsion, and London–van der Waals attraction) and macroscopic interaction (hydration energy) for the edge–face, edge–edge, and face–face platelet interaction system using the model of Mahmood et al. [34]. Details on the mathematical treatment with use of [36–38] are given in the Supplementary information.

The work presented here focuses on (a) FEBEX bentonite-derived montmorillonite colloid stability determined by means of PCS under variation of pH, ionic strength, contact water cation composition (Na^+, Ca^{2+}), and dissolved organic matter (fulvic acid); (b) the montmorillonite pH-dependent edge electrokinetic potential estimation by ζ-potential measurements using the recalculation method proposed by Williams and Williams [39] for different ionic strengths; and (c) comparison of experimentally determined stability ratio W to model predictions using the extended DLVO approach published by Mahmood et al. [34].

2. Materials and Methods

2.1. Colloid Preparation

For the experiments, the FEBEX (full-scale engineered barrier experiment) bentonite from the deposit of Cabo de Gata, Almería (ENRESA, Madrid, Spain) was used [23]. It is described as a smectite-rich bentonite [40]. The bentonite was sieved to obtain the <63 µm size fraction and equilibrated for one week with 1 mol L^{-1} NaCl to transfer the bentonite to its monoionic Na-form. The sodium-exchanged bentonite was washed with deionized (Milli-Q) water to remove excess salt after equilibration. The suspension was centrifuged at 4000 rpm (3360 g) for 40 min Afterwards, the supernatant was discarded and the centrifugate was re-suspended in Milli-Q water. This washing cycle was repeated three times. Each washing step was checked by electrical conductivity measurements, and the final electrical conductivity after all washing cycles was 1.9 µS cm^{-1}. The final supernatant, containing bentonite colloids, was taken as a colloid stock suspension and stored in a refrigerator at 6 °C until performance of the experiments. The cation exchange capacity (CEC) was determined to be 107 meq $(100\ g)^{-1}$. The extracted colloidal fraction consists quantitatively of montmorillonite, as proven by XRD analyses (see Figure S1). The bentonite colloid concentration was determined via alumina ICP-MS measurements. Taking into account the structural formula of FEBEX bentonite given in [23], the bentonite colloid concentration was calculated to be 640 ± 15 mg L^{-1}. The morphology of the bentonite colloids was probed by AFM (see representative particle in Figure S2). The width of the particle was approximately 140 nm and the thickness approximately 2 nm, resulting in a considerably lower aspect ratio than 1:10 found by [41]. The mean bentonite colloid, as determined by PCS, had a diameter of 185 nm with a half-width of 90 nm, recalculated from the polydispersity index of 0.24. That made it smaller than the FEBEX bentonite colloids prepared in $NaClO_4$ with a particle size of 340 ± 10 nm by Mayordomo et al. [21].

2.2. Coagulation Studies

The coagulation rate of the bentonite colloids was determined by photon correlation spectroscopy (PCS) using a ZetaPlus system (Brookhaven Inc., Holtsville, NY, USA). The scattered light was measured perpendicularly to the incident laser beam, and the data evaluation was made by the instrument's built-in software (ZetaPlus Particle Sizing Software Version 2.27, Brookhaven Inc., Holtsville, NY, USA). The hydrodynamic radius (r_h) was calculated from the measured diffusion coefficient (D) by the Stokes–Einstein equation assuming spherical colloid geometry:

$$r_h = \frac{k_B T}{6\pi\eta D} \quad (1)$$

where k_B is the Boltzmann constant, T the absolute temperature, and η is the viscosity of the fluid. The stability ratio is calculated based on the expression given by Kretzschmar et al. [17]:

$$W = \frac{[(dr_h/dt)_{t\to 0}/C]^{(f)}}{[(dr_h/dt)_{t\to 0}/C]} = \frac{r_{fast}}{r_{actual}} \quad (2)$$

whereas W is the stability ratio, C the colloid concentration, and r the coagulation rate. The superscript (f) refers to measurements in the regime of fast, solely diffusion-controlled coagulation in the absence of repulsive energy barriers [17,18,20] (as an example, r_{actual} is given in Figure 1). The coagulation rate is determined for measurements with small hydrodynamic radii, wherein singlet to doublet formation takes place.

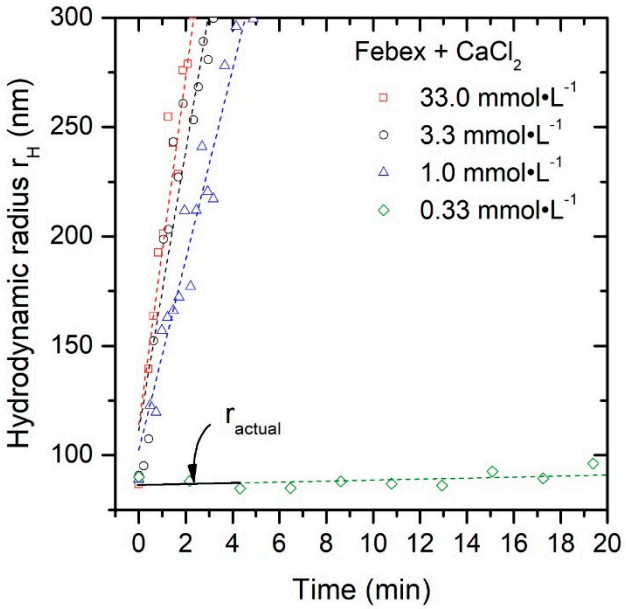

Figure 1. Time-dependent hydrodynamic radius r_H increase for FEBEX bentonite colloids as a function of $CaCl_2$ background electrolyte concentration at pH 8. The actual coagulation rate (r_{actual}) of doublet formation is defined as slope of the time-dependent change of the average colloid hydrodynamic radius.

The region where fast diffusion-controlled aggregation takes place is often referred to as critical coagulation concentration (CCC). The advantage of determining colloid stability by means of W is the independency of the observation time used throughout the experiments [25] and the possibility of direct comparison with published literature data.

The stock solution used throughout the coagulation experiments had a concentration of 3.7×10^{-4}% w/w with a pH of 5.9 ± 0.1. Prior to each coagulation experiment, the colloid size of the stock solution was checked directly in the cuvette. Afterwards, to start the coagulation process, the electrolyte solution was added in the quantity necessary to get the desired concentration. The pH was adjusted by addition of analytical grade NaOH. To prevent coprecipitation of calcium carbonate phases, the measurement setup for measurements in $CaCl_2$ electrolyte solution was covered with a CO_2-free atmosphere.

For each measurement point, an accumulation period of 10 s was set in the software program. The measurement was stopped when the particle size reached approximately 1000 nm. Experiments where this size was reached in t < 180 min were carried out consequently in a single 5 mL cuvette. After removing the cuvette from the PCS, the pH was checked with a Ross-electrode.

Long-term experiments with t > 180 min were performed in 20 mL bottles. The solutions were mixed in these bottles and an aliquot of the mixed solution was transferred into a cuvette for the

particle size measurement. Ten measurements each with a 40-s period were combined into one data point. The aliquot was transferred back to the experimental bottle and the pH adjusted. This cycle was repeated until the particle size reached approximately 1000 nm. The monitoring time of the slow aggregation experiments covers hours to weeks.

2.3. Surface Potential Determination

The electrophoretic mobility μ was measured with the ZetaPlus system using the PALS Zeta Potential Analyzer Software (Version 3.13, Brookhaven Inc., Holtsville, NY, USA) setting the data acquisition criterion to a target residual of 0.02. The ζ-potentials measured in this study were calculated from electrophoretic mobility measurements using Smoluchowski's equation [25]:

$$\zeta = \mu\eta/\varepsilon_r\varepsilon_0 \quad (3)$$

where ε_r is the relative permittivity of water, ε_0 the dielectric permittivity of vacuum, and η the viscosity.

For model calculations, the measured ζ-potential was inserted as an approximation of the surface potential. Due to the lower scatter angle (22°) in the electrophoretic mobility measurements, the FEBEX bentonite colloid concentration was raised to 4×10^{-3}% w/w.

In order to estimate the swelling bentonite colloid edge electrokinetic potential, the ζ-potential of silica and alumina was combined, as proposed by Williams and Williams [39]. The authors are aware of the simplicity of this approach. However, new AFM surface force distance measurements published in the literature focus on non-swelling kaolinite type 1:1 clay minerals to directly measure the basal plane surface charge [42]. Even the direct edge-charge measurement of resin-embedded, ultra-microtome cut kaolinite has been reported [43]. However, the problem remains regarding the transferability of such investigations to a swelling 2:1 clay mineral showing delamination in contact with water and permanent charge due to isomorphous substitution. Therefore, in this study, the authors used the qualitative to semi-quantitative approach mentioned above, while having in mind the oversimplifications made.

The silica and α-alumina stock solutions are prepared by suspending Aerosil90 (Degussa) and TM-DAR (Taimicron) powder, respectively, in Milli-Q water. The bentonite edge electrokinetic potential is calculated with the ratio between silica and alumina given in the structural formula of FEBEX bentonite [23]:

$$\zeta_{edge} = 0.72 \cdot \zeta_{silica} + 0.28 \cdot \zeta_{alumina} \quad (4)$$

The pH range in all measurements varies from 6 to 10. It is adjusted by adding analytical grade NaOH. For the measurements in $CaCl_2$ electrolyte solution, the measurement setup is covered with a CO_2-free atmosphere to prevent coprecipitation of calcium carbonate phases.

2.4. Scanning Transmission X-Ray Microscopy (STXM) Studies

Two samples of bentonite colloids with the addition of 1 mg L^{-1} dissolved organic carbon (DOC by fulvic acid GoHy-573FA [44]) were coagulated with $CaCl_2$ at a concentration of 0.33 mmol L^{-1} at pH 6 and pH 8. The solution is ultra-centrifuged for 1 h at 90,000 rpm (502,135 g). The concentrated settlement was used for the sample preparations.

Carbon K-edge near edge X-ray absorption fine structure (NEXAFS) spectra were measured with a scanning transmission X-ray microscope (STXM) at the STXM-beamline X1A1 (NSLS) built and operated by the University of New York, in Stony Brook. The principle of the method is described in detail elsewhere [45]. The absorption by different carbon structures follows the Lambert–Beer law; i.e., the absorption is directly proportional to the mass absorption coefficients of different carbon functionalities as a function of the X-ray wavelength. The optical density (OD) is equal to the product of sample thickness d, the sample density ρ, and the mass absorption coefficient μ(E), which is related to the quotient of the incident flux on the sample I_0(E) and the flux detected behind the sample I(E) via:

$$\mathrm{OD} = -\ln\left[\frac{I(E)}{I_0(E)}\right] = \mu(E) \times \rho \times d \quad (5)$$

STXM sample preparation was performed by drying 1 µL of concentrated settlement on an Si_3N_4 window (100 nm thick). The spectra were extracted from images taken at different energies across the absorption edge (so-called stacks) after aligning them using cross-correlation [46]. Image regions free of particles give the $I_0(E)$ information. Energy calibration of the spherical grating monochromator was achieved by using the photon energy of the CO_2 gas adsorption band at 290.74 eV [47]. For comparison of different NEXAFS spectra, all spectra were baseline-corrected and normalised to 1 at 295 eV prior to peak fitting and deconvoluted following the procedure described in detail elsewhere [48,49].

3. Results and Discussion

3.1. Colloid Stability

Colloid stability measurements were performed by measuring the time-dependent change of the average colloid's hydrodynamic radius. An electrolyte-concentration-dependent coagulation rate was observed, as expected (see Figure 1). Using $CaCl_2$ as the background electrolyte solution at pH 8, the fastest observed coagulation was at a concentration of ≥33 mmol L^{-1}. When lowering the electrolyte concentration to 3.3 mmol L^{-1}, no decrease in the detected coagulation rate could be observed within the uncertainty. A first significant drop in coagulation rate occurred when the electrolyte concentration was furthermore lowered to 1 mmol L^{-1}, since the repulsive forces between bentonite platelets increased. The reduction of the background concentration to 0.33 mmol L^{-1} increased the repulsive forces even further, leading to a very slow coagulation.

The stability ratio W for each coagulation experiment under constant pH was calculated using Equation (2) and plotted against the concentration for the adjusted pH values (see Figure 2). The observed steep slopes of colloid size increased for concentrations above 1 mmol L^{-1} $CaCl_2$ (Figure 1), resulting in a W between 1 and 2, whereas the critical coagulation concentration (CCC) was determined with W transitions from higher values to 1. Taking into account the uncertainties in the linear slope analysis of the measured data, a W between 1 and 2 has to be considered as CCC in this study. This is indicated as a grey shaded area in Figure 2. For lower background electrolyte concentrations, the stability ratio W increases, which means that not every colloid–colloid collision results in a doublet formation. Taking the crossover of the linear regressions in the log–log plots of Figure 2 for the different pH values investigated, a pH-independent CCC for $CaCl_2$ of 1 mmol L^{-1} can be determined for FEBEX bentonite-derived colloids (see Figure 2a). This value correlates well with the observations made by the Swedish nuclear fuel and waste management company SKB (Svensk Kärnbränslehantering AB) [50]: that the stability of suspended colloids is significantly decreased and the stability of the buffer and backfill is enhanced if the concentration of divalent cations exceeds 1 mmol L^{-1}. SKB 50], therefore, defines a safety function indicator of $[M^{2+}] > 1$ mmol L^{-1} for bentonite buffer stability and an overall ionic strength in the geosphere of $\sum_q [M^{q+}] > 4$ mmol L^{-1} charge equiv [51]. The Ca-CCC found in this study is also in good agreement with published data by Hetzel and Doner for montmorillonite (SWy-1) and beidellite [52], by Séquaris for Na-montmorillonite at pH 9 and 10 [53], by Sellin et al. for B75 bentonite [54]. It is slightly higher than the published values of 0.4 mmol L^{-1} from Lagaly and Ziesmer [55] for 0.025% w/w Na-montmorillonite (Wyoming, M40A); and 0.3 mmol L^{-1} from Chheda et al. [56] for 0.015% w/w Na-montmorillonite (Fischer), and Missana et al. for Na-FEBEX [22] (see Figure 3a). Comparing the layer electrokinetic potential of the FEBEX bentonite colloids determined to be 0.37 eq/formula unit [57] with the variation generally found for montmorillonites of 0.25–0.4 eq/formula unit [58] and the layer electrokinetic potential of 0.28–0.31 eq/formula unit found for Wyoming M40A montmorillonite [55], FEBEX bentonite can be considered as a highly charged montmorillonite. However, the difference in overall layer electrokinetic potential seems not to have a significant influence on the determined Ca-CCC. Since the electrokinetic potential of the tetrahedral layer is not determined, a conclusion cannot drawn on the influence of the tetrahedral layer electrokinetic potential on the colloid stability, although [29–31] report an influence of the tetrahedral layer electrokinetic potential on the rheological properties of montmorillonite.

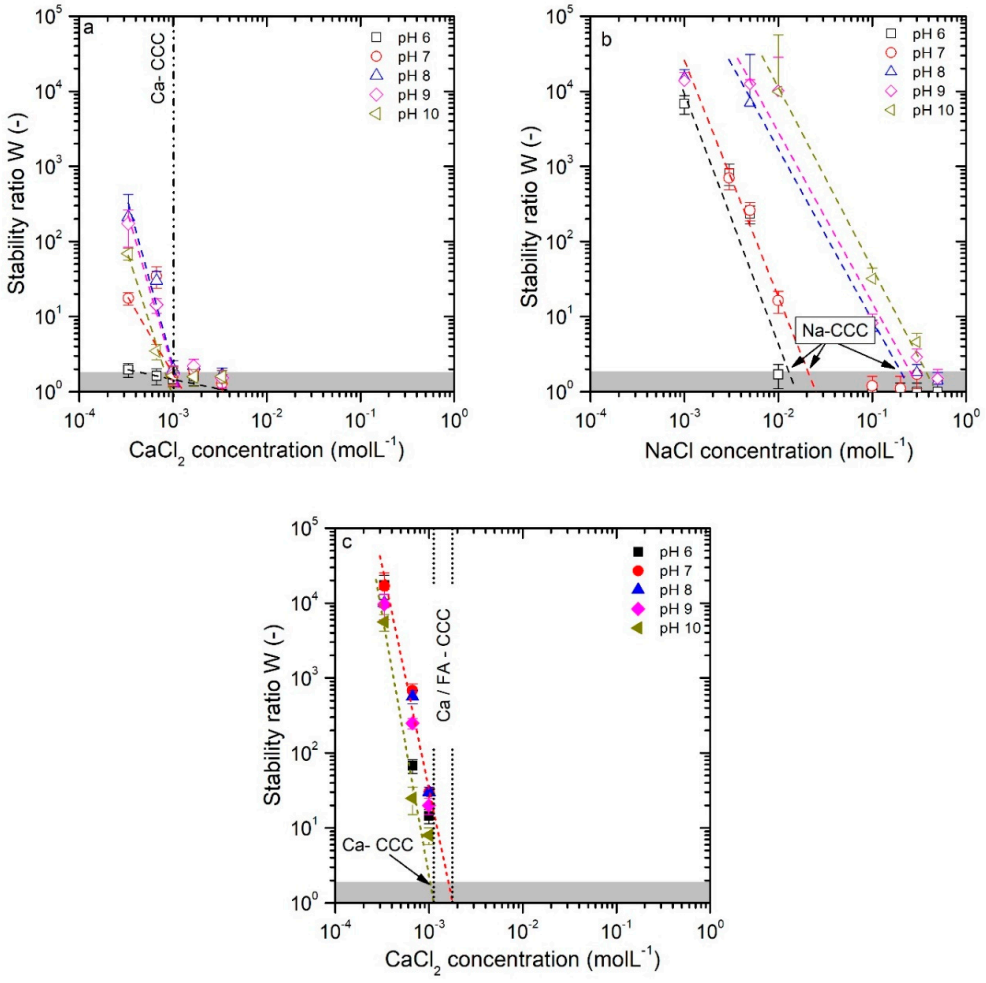

Figure 2. Stability ratio W of FEBEX bentonite colloids is plotted against the electrolyte concentration for $CaCl_2$ in (**a**) and (**c**) as well as NaCl in (**b**). The critical coagulation concentration (CCC) was determined, in which W transitions from higher values to 1. The grey shaded area at the bottom of each graph is considered to show values for the CCC due to errors in stability ratio measurements. The influence of addition of 1 mg·L^{-1} DOC (GoHy-573 FA) on W for all measured concentrations is depicted in graph (**c**).

While using NaCl as the background electrolyte, the calculated W values are plotted against the concentration in Figure 2b. As expected for a 1:1 background electrolyte, in the NaCl systems, the concentrations required to induce FEBEX bentonite coagulation are much higher than using $CaCl_2$ as the background electrolyte, following, in general, the trend predicted by the Schultz–Hardy rule [25]. However, the concentrations are found to be not inversely proportional to the sixth power of the cation valence. In contrast to the Ca-CCC, the Na-CCC is clearly dependent on the pH value of the system with an Na-CCC of 15 ± 5 mmol L^{-1} at pH 6, 20 ± 5 mmol L^{-1} at pH 7, 200 ± 50 mmol L^{-1} at pH 8, 250 ± 50 mmol L^{-1} at pH 9, and 350 ± 100 mmol L^{-1} at pH 10, respectively. The Na-CCC values determined for the NaCl system are plotted as a function of the pH value in Figure 3b. The determined Na-CCC values for pH 6 and pH 7 are in good agreement with published Na-CCC data for SWy-1 and the beidellite from Hetzel and Doner [52] and Lagaly and Ziesmer [55] for pH 6.5, and Chheda et al. [56] for pH 6.8. Tombácz and Szekeres [59], however, determined Na-CCC values at pH 6 for Wyoming montmorillonite SWy-1 and SWy-2 of 52 mmol L^{-1}—considerably higher than the Na-CCC values observed in this study for FEBEX bentonite. Sellin et al. [54] and Missana et al. [22] determined an Na-CCC below 10 mmol L^{-1} at pH 6.7 and pH 7, respectively.

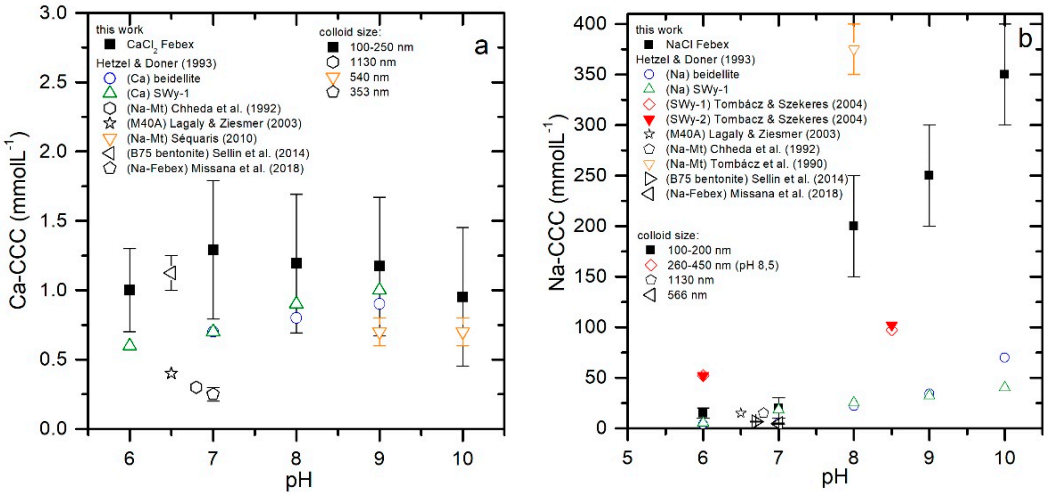

Figure 3. Critical coagulation concentration (CCC) plotted against pH for $CaCl_2$ (**a**) and NaCl (**b**). The Ca-CCC does not change within the analytical uncertainty for the investigated pH range. For comparison, the CCC data and colloid sizes from Hetzel and Doner [52] for montmorillonite (Swy-1) and beidellite; Na-montmorillonite from Séquaris [53]; Na-montmorillonite (Wyoming, M40A) from Lagaly and Ziesmer [55]; Na-montmorillonite (Fischer) from Chheda et al. [56]; Wyoming montmorillonite Swy-1 and Swy-2 from Tombácz and Szekeres [59]; Na-montmorillonite from Tombácz et al. [60]; B75 bentonite from Sellin et al. [54]; and Na-FEBEX from Missana et al. [22] were inserted. The Na-CCC values for pH 6 and 7 are within the range found in the literature, whereas for pH 8 to 10, considerable variation is present. Possible explanations are given in the text.

Theoretical calculations by Liu et al. [61] predict, based on the FEBEX bentonite colloid size of 185 nm (PCS, see Chapter 1.3) and a calculated particle surface area S_p of 8.2×10^4 nm^2 (particle thickness δ_P 2.4 nm), a Na-CCC of 20–30 mmol L^{-1} for pH 5–6.5, which is slightly above the measured values of 15 ± 5 mmol L^{-1} for pH 6.

The observed increase in Na-CCC above the isoelectric point pH_{iep} (see next chapter) of the montmorillonite edges might be explained by a full delamination of the montmorillonite platelets based on the approach of Liu et al. [61]. Asymmetrical flow field-flow fractionation (AsFlFFF) studies of fully delaminated FEBEX bentonite by Bouby [62] have shown a bimodal size distribution varying from 15–300 nm with peak maxima at 40 and 150 nm. Taking a particle thickness δ_P of 1.2 nm for fully delaminated platelets and the AsFlFFF derived, smaller colloid size peak maxima of 40 nm, a Na-CCC of approximately 200 mmol L^{-1} would be predicted, which is in fairly good agreement with the measurements made at pH 8–10. However, it has to be noted that published Na-CCC data in the pH range 8–10 scatter considerably with highest values found by Tombácz et al. [60] of 350–400 mmol L^{-1} at pH 8 and lowest values of 18–40 mmol L^{-1} at pH 8–10 for SWy-1 [52] (see Figure 3b).

A reason for the huge scatter found at high pH can be the difference in sample preparation and measurement techniques used. The different studies cited in this work transformed their clays to their mono-ionic form by exchange with NaCl or $NaClO_4$. The cleaning step mostly includes centrifugation and washing, and dialysis against Milli-Q water [56] or 0.01 mol L^{-1} electrolyte solution [52,59]. Each treatment and the differences in centrifugation times and velocities lead to different clay colloid sizes and thicknesses. Liu et al. [61] predict a particle-size-dependent CCC. The colloid sizes of the cited literature give 260–450 nm at pH 8.5 for SWy-1 [59], 1130 nm [56], 540 nm for Na-montmorillonite [53], and 566 ± 31 nm for Na-FEBEX [22]. These colloid sizes and the given literature CCC values confirm lower CCC values than those measured by this work. However, the higher colloid stability in NaCl electrolyte solution at pH 6 from Tombácz and Szekeres [59] can be explained by steric stabilisation due to the selected solid/liquid ratio of 4% w/w. Other authors include pretreatment with Na_2CO_3 [60] or with citrate/H_2O_2 to remove iron oxides and humic substances [55], which can change the surface and edge properties of the colloids and influence the colloid stability, too.

The addition of 1 mg L^{-1} dissolved organic carbon (DOC) as fulvic acid (GoHy-573FA) increases the colloid stability and the resulting W in $CaCl_2$ background electrolyte solution for the measured pH range (see Figure 2c). Taking the intersection at W = 1 as calcium critical coagulation concentration in presence of fulvic acids (Ca/FA-CCC) for pH 10, only a marginal increase can be detected, which is within the analytical uncertainty. This observation is in line with measurements of Norrfors et al. [19], who could not determine a change in colloid stability by addition of GoHy-573FA to MX-80 bentonite colloids. However, at lower pH values, an increase in the Ca/FA-CCC to values ≤2 mmol L^{-1} could be determined, and therefore 2 mmol L^{-1} was taken as Ca/FA-CCC.

In order to verify the fulvic acid surface association with montmorillonite colloids at pH 6 and 8, aliquots of the investigated suspensions were ultracentrifuged, and the settlements were investigated by carbon K-edge STXM. The STXM method has been tested in various environmental systems, including (a) natural particulate matter of ultra-oligotrophic lakes [63], (b) distribution of natural organic matter in low carbon claystone formations [64], (c) chemical characterisation of natural organic matter, humic and fulvic acids [65], and (d) their fractionation through metal complexation or mineral interaction [65–67], which proved to be a very sensitive technique.

The spectral features observed at the carbon K-edge include an absorption band at 285.2 eV, which is typical for aromatic carbon bonded either to carbon or a proton. The excitation around 286.6 eV is assigned to aromatic carbon bonded to oxygen C(1s) → $\pi^*_{C\text{-}OH}$, as found in phenol or halogenated aromatics. The splitting is due to symmetry reduction and/or chemical shifts (higher electron affinity) associated with the ligand group [68]. The next higher excitation around 287.6 eV is not a π* state but a low-lying 1s carbon transition to a mixture of 3p Rydberg orbital with a symmetrical antibonding C-H* orbital [68], as in aliphatic methyl and methylene groups. The most intense band in all fulvic acids spectra is around 288.2 to 288.8 eV and can be assigned to the large oscillation strength of the $1\pi^*_{C=O}$ of aromatic and aliphatic associated carboxylic groups [69]. An additional transition at around 289.5 eV is typically assigned to the O-alkyl group found in alcohols and carbohydrates.

In comparison to the pure fulvic acid (GoHy-573FA), the carbon K-edge spectra of the FEBEX bentonite colloid-associated organics, both sorbed at pH 6 and pH 8, show significantly different spectra (see Figure 4). The absorption band intensity at 285.2 eV is significantly weaker in the surface-associated organics compared to the pure GoHy-573FA and can be interpreted with a higher number of hydroxyl groups associated to the surface-sorbed aromatic structures, as found in a comparative study between phenols and benzene [70]. This is accompanied by the stronger intensity of the $1\pi^*_{C=O}$ of aromatic and aliphatic-associated carboxylic groups at 288.5 eV and a general higher content of oxygen-containing functional groups (∑(phenol-type + carboxyl-type + carbonyl-type)), as quantified by deconvolution [48] of 81% for pH 6 and 77% for pH 8, respectively. The high oxygen content of surface-associated organics is very comparable with previous studies on natural organics associated with FEBEX bentonite (79%) [13] and significantly higher than the amount of oxygen-containing functional groups found for pure GoHy-573FA with 67% (see Figure 4a). The exact amount of FEBEX bentonite associated with FA cannot be determined within the uncertainty of the DOC measurements and the reproducibility of the sample preparation by ultracentrifugation. The ratio image taken at pH 6 (see Figure 4b) shows organic compounds associated with the FEBEX bentonite colloids as a rather homogeneous surface coverage with some hot spots of high organic carbon concentration. As clearly evidenced by these high-resolution STXM images, the fulvic acids added to the FEBEX bentonite colloid suspension at pH 6 are surface-associated. The observed increase in colloid stability and CCC can therefore be attributed to an increase in magnitude of the negative electrokinetic potential or charge reversal of colloid edge sites.

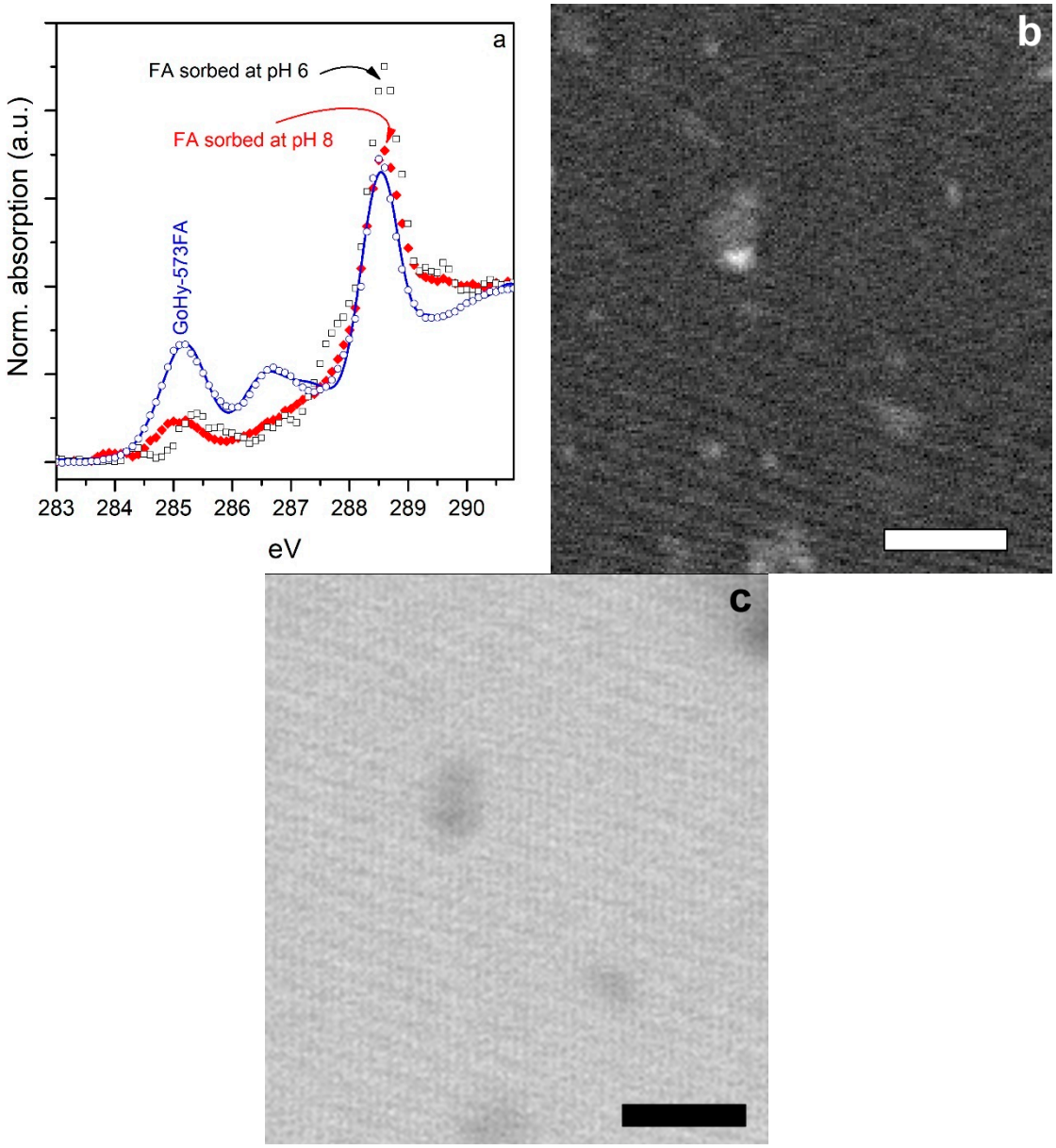

Figure 4. (**a**) Data points of measured carbon XANES spectra of GoHy-573FA starting solution prior to FEBEX bentonite sorption and spectra of organics associated to FEBEX bentonite colloids at pH 6 and pH 8, respectively. The solid line represents a best fit of the 290 eV fulvic acid spectra taking the deconvolution procedure as described in Schäfer et al. [48] and Schäfer et al. [49]. (**b**) Ratio image (−log (I[2 85.3 eV − 295.0 eV]/I_0[283 eV]) of organics associated with FEBEX bentonite colloids at pH 6. Brighter grey values indicate higher concentrations of organic material and show several hot spots of organic material on the clay platelets beside a homogeneous surface coverage. (**c**) STXM image taken at 283 eV below the carbon K-edge, showing absorption of bentonite colloids and aggregates. Scale bars in (**b**) and (**c**) represent 2 µm.

3.2. Surface Electrokinetic Potential Estimation

3.2.1. $CaCl_2$ System

The ζ-potential for FEBEX bentonite colloids in two different $CaCl_2$ background electrolyte concentrations show negative electrokinetic potentials over the investigated pH range from 6 to 10 with a slight decrease of the electrokinetic potential towards lower pH values (see Figure 5a). The FEBEX bentonite colloid edge electrokinetic potentials are estimated using Equation (4): inserting

the ζ-potential measurements of silica and α-alumina colloids (see Figure 5b). The estimated bentonite edge electrokinetic potential using 33 mmol L^{-1} $CaCl_2$ as background electrolyte shows an isoelectric point pH_{iep} of ~9.4 and positive edge electrokinetic potentials below the pH_{iep}. The expected low colloid stability due to the positive edge electrokinetic potentials is qualitatively in line with the observed fast coagulation (W = 1) based on the stability measurements in this $CaCl_2$ background electrolyte concentration range (see Figure 2a). For a $CaCl_2$ background concentration of 0.33 mmol L^{-1}, a slow increase in colloid size is observed in the coagulation experiments (see Figure 1). The estimated edge electrokinetic potential as well as the measured ζ-potential for the FEBEX bentonite are both negative for this background electrolyte concentration.

Table 1. Measured stability ratio $W_{measured}$ with and without addition of 1 mg L^{-1} DOC (GoHy-573 fulvic acid, FA) for $CaCl_2$ electrolyte solution. Theoretical W_{DLVO} values calculated with Equation (6) and $W_{DLVO,\ best\ fit}$ values derived from fitting the surface electrokinetic potential of the FEBEX bentonite colloid (see lines in Figure 5a).

Concentration (mmol·L^{-1})	pH	$W_{measured}$	W_{DLVO}	$W_{DLVO,\ best\ fit}$	$W_{measured\ FA}$
0.33	6	2 ± 0.4	2	2	17,373
0.33	7	18 ± 3.0	6	18	16,950
0.33	8	211 ± 20	19	210	10,000
0.33	9	173 ± 89	66	174	9596
0.33	10	69 ± 12	283	68	5614
33	6	1 ± 0.2	1	1	n.m.
33	7	1 ± 0.2	1	1	n.m.
33	8	1 ± 0.2	1	1	n.m.
33	9	1 ± 0.2	1	1	n.m.
33	10	1 ± 0.2	1	1	n.m.

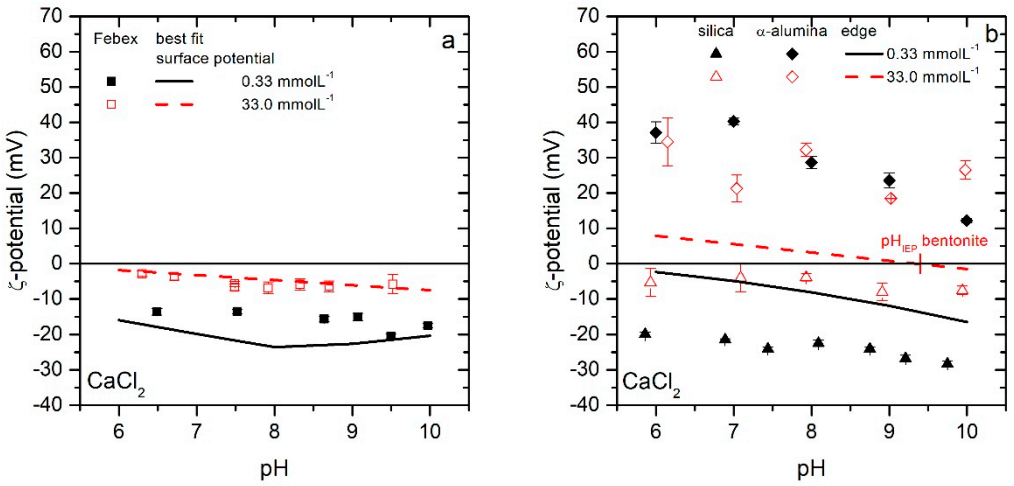

Figure 5. (**a**) FEBEX bentonite colloid ζ-potential in $CaCl_2$ background electrolyte solution. Data points represent the measured ζ-potentials at 0.33 mmol·L^{-1} (filled squares) and 33 mmol·L^{-1} (open squares) as a function of pH. The solid lines represent the best fits for the surface potentials to reproduce the measured stability ratios, as given in Table 1. The value of the surface electrokinetic potential is given in Table S6. (**b**) Silica (triangles) and α-alumina (diamonds) ζ-potential in $CaCl_2$ background electrolyte solution. Data points represent the measured ζ-potentials at 0.33 mmol·L^{-1} (filled) and 33 mmol·L^{-1} (open) as a function of pH. The lines indicate the estimated edge electrokinetic potential for the two electrolyte concentrations using Equation (4).

3.2.2. NaCl System

The FEBEX bentonite ζ-potential for the NaCl background electrolyte system (see Figure 6a) is considerably (≈−15 to −25 mV) lower in value but higher in magnitude compared to the $CaCl_2$

system (see Figure 5a). Due to the data deviation in the ζ-potential measurements, the linear fits using 1 mmol L^{-1} and 100 mmol L^{-1} NaCl background electrolyte, respectively, do not show any significant difference (see Figure 6a). These linear fits are used as face surface potential in the successive modelling. The estimated edge electrokinetic potential as well as the ζ-potential of silica and α-alumina are plotted in Figure 7a. For the sensitivity analysis of the appropriateness of the model alumina mineral for edge electrokinetic potential estimation, the edge electrokinetic potential calculation with α-alumina data from this paper is compared with α-alumina data (see Figure 7a) published by Kupcik et al. [71] (α-$alumina_{Kup}$) and γ-alumina data (see Figure 7b) published by de Lint et al. [72]. The difference between the pH_{iep} of the α-alumina (~9.7) and of α-$alumina_{Kup}$ (8.6–8.8) can be explained by different sample preparation methods. One batch sample is prepared for each measured pH value, while Kupcik et al. [71] titrated their solution under CO_2-exlusion and directly measured the ζ-potential. The pH_{iep} of both α-alumina measurements lie within the range of pH 8–10, as given in the literature [73,74]. The determined γ-alumina pH_{iep} of 8.7 is as well within the values given in the literature. The estimated edge electrokinetic potential based on Equation (4) for the 100 mmol L^{-1} NaCl background electrolyte shows a comparable pH_{iep} and ζ-potential curve for the α-alumina and γ-alumina, while α-$alumina_{Kup}$ has a significantly lower pH_{iep}. In the case of 1 mmol L^{-1} NaCl background electrolyte, an edge electrokinetic potential pH_{iep} of ~6 is found in the case of α-alumina (see Figure 7a) and of ~5.5 for α-$alumina_{Kup}$ (see Figure 7b), whereas calculations of the bentonite edge electrokinetic potential using γ-alumina revealed a negative edge electrokinetic potential over the entire investigated pH range (see Figure 7c). The above-mentioned discrepancy between α and γ-alumina is almost negligible at pH 9–10, but becomes more pronounced with decreasing pH values, especially at pH 7–8 with a maximum difference of ~10 mV.

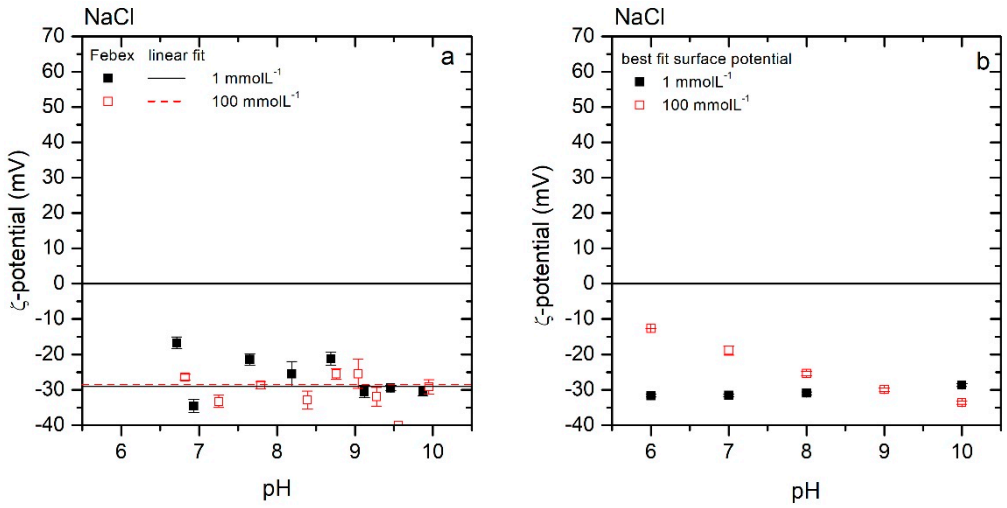

Figure 6. FEBEX bentonite colloid ζ-potential in NaCl electrolyte solution (**a**). Data points represent the measured ζ-potential at 1 mmol·L^{-1} (filled squares) and 100 mmol·L^{-1} (open squares). The lines indicate the linearly fitted pH and ionic-strength independent surface potential, as indicated in Table S2. The symbols in (**b**) represent the best fit for the surface electrokinetic potential to recalculate the observed stability ratio given in Table 2. The value of the surface electrokinetic potential is given in Table S6.

The calculated positive edge electrokinetic potentials for 100 mmol L^{-1} NaCl at pH 6–7 correspond to the coagulation observed under these experimental conditions. Based on the experimentally determined Na-CCC of 15 mmol L^{-1} for pH 6, the edge electrokinetic potential estimation based on γ-alumina seems to better represent the FEBEX bentonite coagulation behaviour. In the case of α-alumina, the edge electrokinetic potential already reaches charge neutrality using a 1 mmol L^{-1} NaCl background electrolyte at pH 6, and strong coagulation should be expected. However, the general

trend of increased bentonite stability with decreasing NaCl concentration can directly be deduced from the more negative values of the ζ-potential.

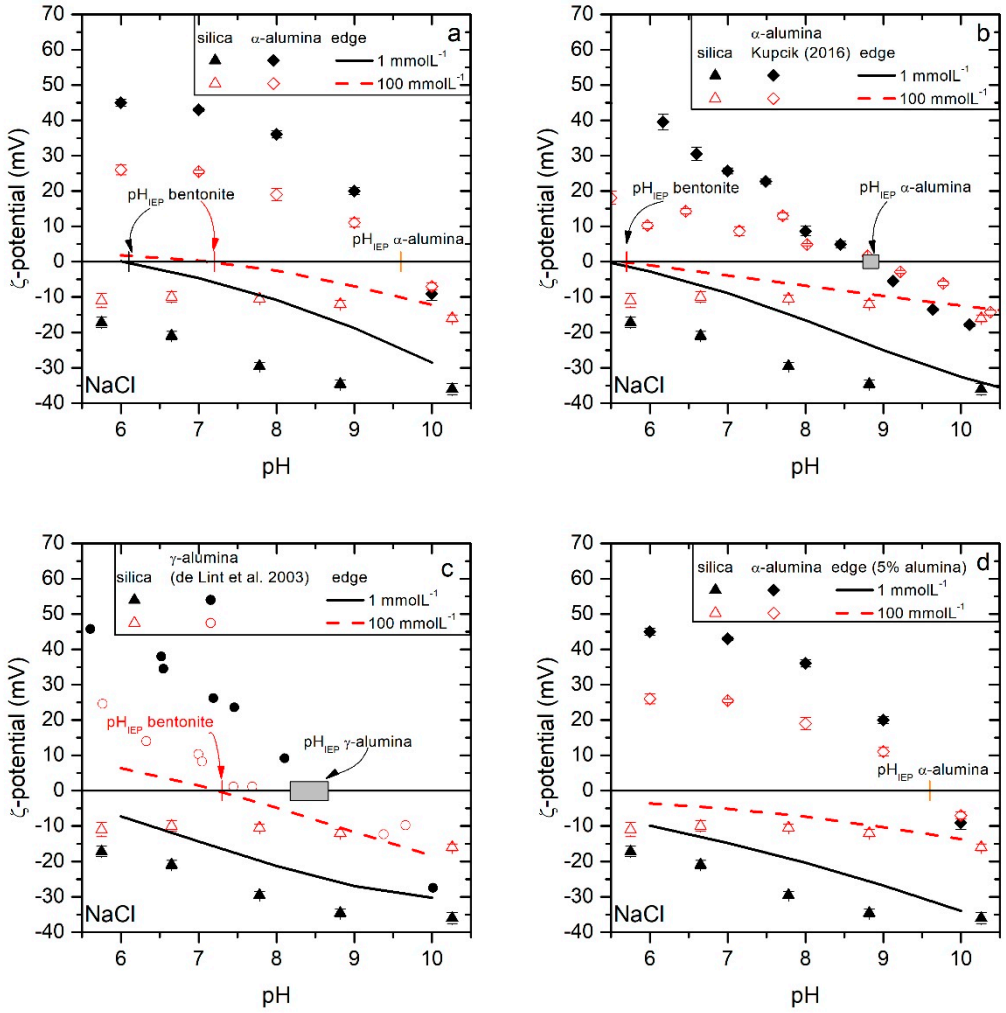

Figure 7. Measured silica (triangles) and α-alumina (diamonds) ζ-potentials at 1 mmol·L^{-1} (filled symbols) and 100 mmol·L^{-1} (open symbols) are plotted in (**a**). The lines indicate the estimated edge electrokinetic potential with a structural Al-ratio of 10.32% for the two electrolyte concentrations. The edge electrokinetic potential is also estimated using α-alumina ζ-potentials taken from Kupcik et al. [71] (**b**) and γ-alumina ζ-potential taken from de Lint et al. [72] (**c**). For Figure (**d**), the edge electrokinetic potential is calculated with a structural Al-ratio of 5%.

So far, the estimated edge electrokinetic potential was calculated using Equation (4) with a structural Al-ratio (Al mass/mass of all components) of 10.32%, which was derived by the FEBEX empirical formula given in [23]. However, the structural Al-ratio of FEBEX bentonite varies in the literature. In this work, the Al-ratio was determined via gravimetric and ICP-MS-analysis and was found to be 8.09%, whereas Missana et al. [75] gave a structural Al-ratio of FEBEX bentonite colloids of 6.9%. To evaluate the impact of a lower Al-ratio in the edge electrokinetic potential estimation, a lower structural Al-ratio of 5% was chosen, and the edge electrokinetic potential was calculated as in Equation (4) with a silica/alumina-ratio of 87.4% silica and 12.6% alumina (see Figure 7d). For the estimation of 5% edge alumina, the α-alumina ζ-potential determined in this work was used and shows for both background electrolyte concentrations, a negative edge electrokinetic potential.

3.2.3. Surface Potentials

The face surface potentials of FEBEX bentonite colloids are estimated from measured ζ-potentials (see linear fit in Figure 6a). A ζ-potential measurement is, due to the distance of the shear plane to the surface, always an approximation of the real surface potential. This real surface potential is usually higher in magnitude (more negative) than the measured ζ-potential. The face surfaces have always a negative electrokinetic potential due to isomorphous substitution. Possible charge heterogeneities due to different edge and surface electrokinetic potentials cannot be determined by ζ-potential measurements. Since in this work the edge electrokinetic potential is estimated by using different alumina and silica ζ-potentials, possible charge heterogeneities are accounted for.

3.3. DLVO Model Predictions

In a next step the authors calculated the interaction energy barrier based on the extended DLVO approach of Mahmood et al. [34] with use of [36–38], as detailed in Chapter S1 of the Supplementary information (for the measured bentonite ζ-potentials (used as face electrokinetic potentials), see Table S2), and the estimated edge electrokinetic potential for which ζ-potentials with α-alumina, α-alumina$_{Kup}$ and γ-alumina as well as with a lower structural Al-ratio of 5% (see Tables S3–S5, Supplementary information) are used as input parameters. The total interaction energy is a sum of the different energy contributions of edge–edge, edge–face, and face–face interactions.

Based on V_{max}, and the height of the calculated primary energy maximum in the total interaction energy, the stability ratio W_{DLVO} is calculated by the equation given in Lewis [76]:

$$W_{DLVO} = \exp\left(\frac{V_{max}/k_BT}{2\kappa r_H}\right) \quad (6)$$

where k_B is the Boltzmann constant, T the absolute temperature, k the reciprocal double layer thickness (Equation (S5), Supplementary information), and r_H the hydrodynamic radius of the colloid. The results show that the general trend of stability ratio variations is qualitatively predicted, but the calculated stability ratios W_{DLVO} under or overpredict the measured colloid stability $W_{measured}$, sometimes by orders of magnitude (see Tables 1 and 2).

Table 2. Measured stability ratio $W_{measured}$ for NaCl electrolyte solution. Theoretical W_{DLVO} values calculated with Equation (6) for different edge electrokinetic potentials estimated with α-alumina (see Figure 7a), α-alumina$_{Kup}$ (see Figure 7b), γ-alumina (see Figure 7c), and 5% structural Al-ratio (see Figure 7d). $W_{DLVO,\ best\ fit}$ represents the arithmetic mean of the obtained results for the four edge electrokinetic potentials and the best fit surface electrokinetic potential (see Figure 6b).

Concentration (mmol·L^{-1})	pH	$W_{measured}$	W_{DLVO} α-Al_2O_3	W_{DLVO} α-Al_2O_3 Kup	W_{DLVO} γ-Al_2O_3	W_{DLVO} 5% α-Al_2O_3	$W_{DLVO,\ best\ fit}$ Al_2O_3
1	6	6720 ± 1877	572	687	619	1202	6717 ± 210
1	7	9810 ± 220	784	1102	1057	1913	9918 ± 367
1	8	12,900 ± 4138	1303	2306	2407	3513	13,028 ± 449
1	9	16,000 ± 3856	2898	6120	7219	7700	16,124 ± 454
1	10	19,100 ± 4604	9622	16,840	25,077	20,522	19,236 ± 567
100	6	1 ± 0.2	9	9	9	9	1 ± 0.01
100	7	2 ± 0.3	9	9	9	9	2 ± 0.01
100	8	5 ± 0.4	9	9	9	9	5 ± 1
100	9	13 ± 1	9	9	9	9	12 ± 1
100	10	34 ± 5	10	10	10	10	31 ± 3

3.3.1. Variation of Surface Electrokinetic Potential ($W_{DLVO,\ best\ fit}$)

In order to estimate the sensitivity of the DLVO model, the calculated edge electrokinetic potential is kept constant, while the FEBEX bentonite face electrokinetic potential is varied until the best fit $W_{DLVO,\ best\ fit}$ values given in Tables 1 and 2 are obtained. For $CaCl_2$, only one edge potential is determined (see Figure 5); therefore, only one value for $W_{DLVO,\ best\ fit}$ is given in Table 1. For NaCl,

the best fit is calculated for the edge electrokinetic potentials with α-alumina, α-alumina$_{Kup}$, γ-alumina, and 5% structural Al-ratio. From these four obtained best fit values, the arithmetic mean is given in Table 2. The derived best fit bentonite face ζ-potentials are plotted as lines in Figure 5a and squares in Figure 6b. The respective values are given in Table S6. To fit the $W_{measured}$ values, the surface potential is varied at a maximum of ±4.1 mV for $CaCl_2$ electrolyte at 0.33 mmol L^{-1} and ±15.9 mV using NaCl electrolyte at 100 mmol L^{-1}. The estimated surface ζ-potentials are physically realistic, since the derived best fit surface electrokinetic potential is more negative using 100 mmol L^{-1} than using 1 mmol L^{-1}. Only at pH 10, is a lower ζ-potential determined in the linear approximation for 100 mmol L^{-1}, which is physically not correct.

3.3.2. Interaction Energy

The different energy contributions from the edge–edge (EE), edge–face (EF), and face–face (FF) interactions are the results of the interaction energy calculations based on the DLVO model of Mahmood et al. [34] and are plotted in Figure 8 as a function of the separation distance given in nm. The total interaction energy (see Figure 8g,h) is the sum of all calculated interaction energy contributions. The energy barrier V_{max} is with higher pH values under constant ionic strength (see Figure 8g), and therefore, based on Equation (6), an increased colloid stability is expected. Regarding the EE and EF interaction, an attractive interaction energy (see Figure 8a,c) is calculated for pH ≤ 8 (EE) and pH ≤ 7 (EF), and thus a fast coagulation in the EE or EF mode is expected. In the total interaction energy calculation (see Figure 8g), an energy barrier V_{max} still exists, and therefore high stability ratios $W_{DLVO,best\ fit}$ are predicted. Regarding the face–face (FF) interaction energy using 1 mmol L^{-1} NaCl background electrolyte (see Figure 8e), exclusively repulsive forces are predicted over the entire pH range with only minor variations, as expected from the fitted surface potential (see Figure 6b). Due to the more negative surface potential of −31.7 mV at pH 6 compared to −28.7 mV at pH 10, the interaction energy increases with lower pH values. The FF mode calculation made in this study is comparable to standard DLVO theory calculations and demonstrates the insensitivity to predict colloidal stability of heterogeneously charged colloids, as already pointed out by Missana and Adell [18].

In the case of 100 mmol L^{-1} NaCl background electrolyte, the best fit bentonite surface potential (see Figure 6b) decreases from pH 8 (−25 mV) to pH 6 (−12 mV), respectively, and for pH 10 it is slightly lower than using 1 mmol L^{-1} NaCl background electrolyte. At higher salt concentration, the electric double layer is significantly compressed and has no influence at distances >5 nm away from the surface, and therefore, attractive forces based on the van der Waals attraction are calculated. The short range repulsive interactions are not strong enough to build up an energy barrier in the EE and EF mode (see Figure 8b,d). The attractive van der Waals interaction is also responsible for the secondary minimum in the FF mode (see Figure 8f). Furthermore, the comparatively higher ionic strength of the solution, and therefore a larger k, are responsible for an even shorter FF interaction energy range. A decreasing $V^{FF}{}_{max}$, an increasing secondary minimum of $V_{min} = -48\ Jk_B{}^{-1}T^{-1}$ at 100 mmol L^{-1}, and a distance from the surface of 4.8 nm to $V_{min} = -63\ Jk_B{}^{-1}T^{-1}$ at 200 mmol L^{-1} with a distance of 4 nm, were calculated.

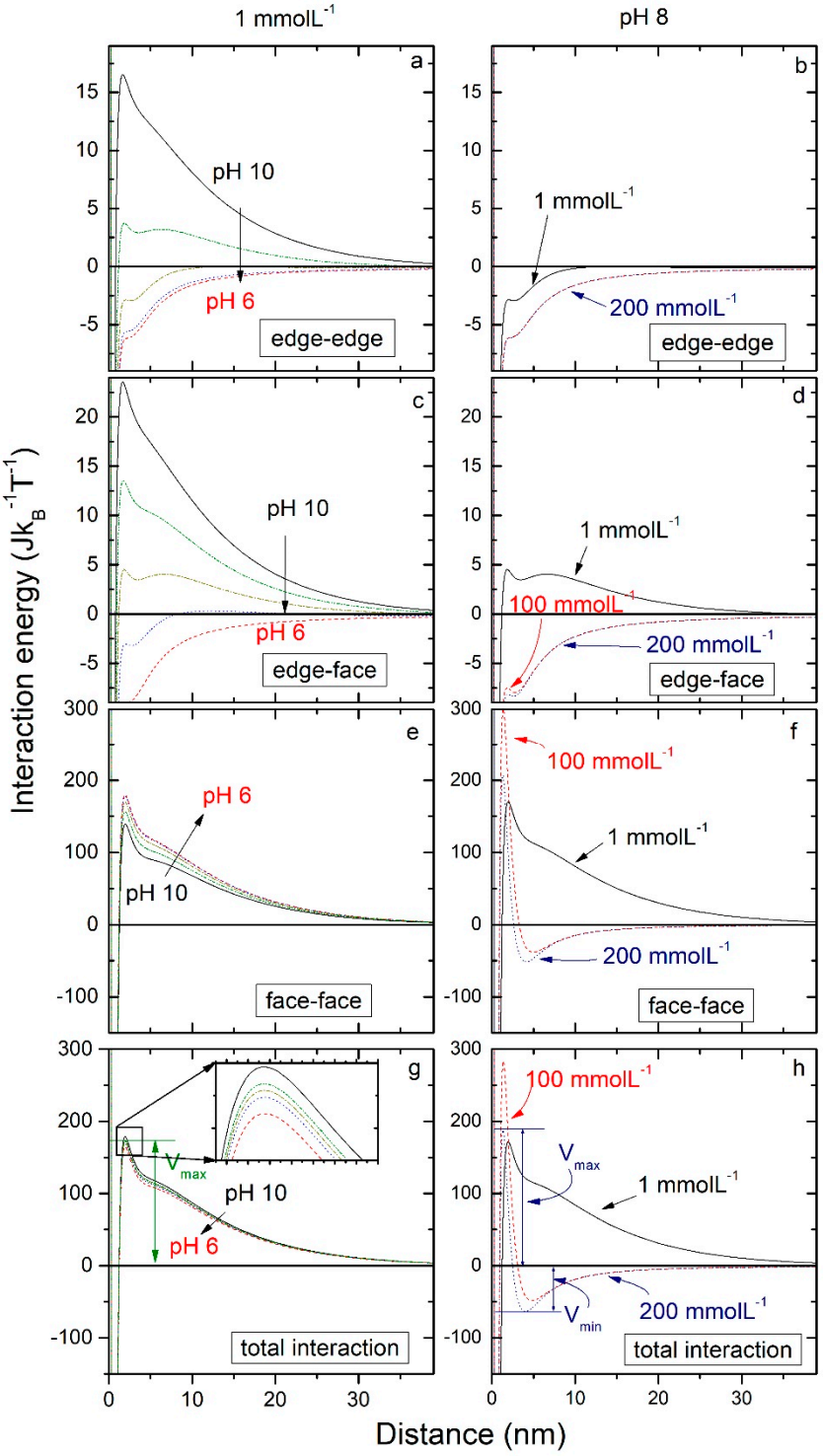

Figure 8. Interaction energy calculated for edge–edge (**a**,**b**), edge–face (**c**,**d**), face–face (**e**,**f**), and total (**g**,**h**) interaction for FEBEX bentonite colloids and 1 mmol L^{-1} NaCl electrolyte solution as a function of pH (left) and different background electrolyte concentrations at pH 8 (right) for the best fit surface potentials (see Figure 6b) and the edge electrokinetic potential calculated with α-alumina (see Figure 7a).

3.3.3. Particle Geometry Assumption

The assumption regarding the clay mineral geometry was based on the particle geometry observed in AFM measurements where an aspect ratio between height and length of 1:55 was found (see Figure S2). The particle count n in this measurement was low (n = 10). With a higher statistic of n = 200,

Plaschke et al. [41] derived an aspect ratio of 1:10 for FEBEX bentonite colloids. A change in the particle geometry assumption to a higher edge surface area will influence the total interaction energy. It will, however, still be controlled by the much higher repulsive forces between the particle faces. For a half cylinder of 1 nm (the radius used throughout the model calculations), a total interaction energy of 153 $Jk_B^{-1}T^{-1}$ can be calculated (see Figure 9). If the radius of the half cylinder is varied between 1 and 20 nm, the total interaction energy increases to 209 $Jk_B^{-1}T^{-1}$ for a radius of 20 nm.

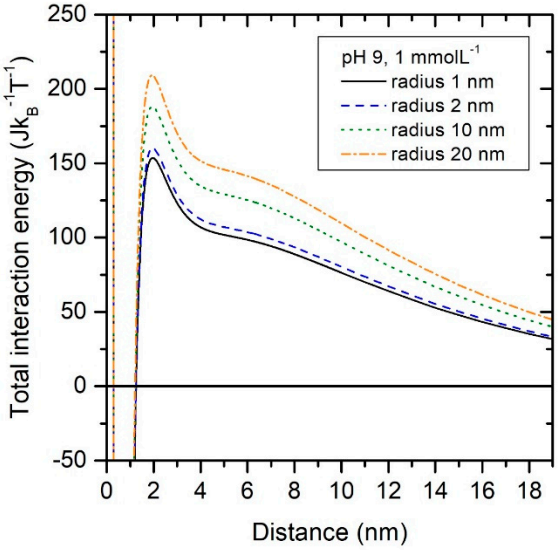

Figure 9. Variation of the edge radius in DLVO calculations. The best fit surface potential of FEBEX bentonite colloids (see Figure 6b) and the estimated edge electrokinetic potential of α-alumina (see Figure 7a) at pH 9 and a background electrolyte concentration of 1 mmol L^{-1} are used.

3.3.4. Energy Barrier Minima

The DLVO calculations show a secondary minimum using NaCl background electrolyte solutions >1 mmol L^{-1} (see Figure 8h). For two colloids, an agglomeration into the primary minimum (overcome energy barrier) or into the secondary minimum (energy barrier not passed) depending on the height of the energy barrier and the depth of the secondary minimum can be distinguished. Marmur [77] found an agglomeration solely into the secondary minimum at a depth of 6–7 $Jk_B^{-1}T^{-1}$. Molina-Bolívar et al. [78] showed that the approach of latex colloids into the secondary or primary minimum also depends on the colloid size. Small colloids (≤100 nm) solely aggregate into the primary minimum, while bigger colloids (>200 nm) at an electrolyte concentration <200–400 mmol L^{-1} stay in the secondary minimum. At higher electrolyte concentrations (>200–400 mmol L^{-1}) they overcome the energy barrier and aggregate into the primary minimum. Molina-Bolívar et al. [78] found for 200 nm latex colloids, with a colloid size comparable to the FEBEX bentonite colloids used in this study, an aggregation into the secondary minimum up to a NaCl electrolyte concentration of 250 mmol L^{-1}. Calculations by Séquaris [53] also show for soil colloids with a colloid radius of 200–300 nm, a dominant aggregation into the secondary minimum with $CaCl_2$ electrolyte solution.

The energy barrier height can be overcome by thermal motion of the colloids if it lies between $V_{max} \leq 1$ $Jk_B^{-1}T^{-1}$ [79] and $V_{max} \leq 10$ $Jk_B^{-1}T^{-1}$ [80]. The depth of the secondary minimum is given by different authors to lie between $|V_{min}| \approx$ 6–7 $Jk_B^{-1}T^{-1}$ [77] and $|V_{min}| \approx$ 10–20 $Jk_B^{-1}T^{-1}$ [81,82]. A stability ratio W_{sec} for the agglomeration into the secondary minimum can be calculated after Hogg and Yang [83] with Equation (7). If a secondary minimum ≥ 1 $Jk_B^{-1}T^{-1}$ is calculated, Equation (8) of Bagchi [79] can be used.

$$W_{sec} = \frac{1}{1 - \exp(V_{min}/k_B T)} \quad (7)$$

$$W_{sec} = \frac{1}{1 - \exp(1 - V_{min}/k_B T)} \quad (8)$$

Using Equations (7) and (8), the CCC with $W_{sec} \approx 1$ $Jk_B^{-1}T^{-1}$ is reached at $|V_{min}| \approx 5$ $Jk_B^{-1}T^{-1}$. The model calculations show a secondary minimum of $|V_{min}| > 20$ $Jk_B^{-1}T^{-1}$ for NaCl electrolyte concentrations of 100 and 200 mmol L^{-1} (see Figure 8h). At 100 mmol L^{-1}, the measured stability ratios vary over $W_{measured}$ = 1–34 at pH 6–10 (see Table 2). In the presented colloid stability measurements, differentiation between an agglomeration in the secondary or primary minimum is not possible. Since an instantaneous agglomeration was observed in the coagulation studies between pH 6 and 7 with NaCl electrolyte concentrations of 100 mmol L^{-1}, an aggregation into the secondary minimum cannot be neglected; they also cannot since the theoretical calculations predict a secondary minimum.

3.3.5. Fit of CCC over V_{max}

Figure 8b,d,f,h include the calculated interaction energies of a 200 mmol L^{-1} electrolyte solution, which is the determined Na-CCC at pH 8 (see Figure 3b). It is shown that the CCC criterion of $V_{max} \approx 1$ $Jk_B^{-1}T^{-1}$ or $V_{max} \approx 10$ $Jk_B^{-1}T^{-1}$, respectively, is not kept. As a test for the DLVO model, the electrolyte concentration with constant face and edge electrokinetic potential is varied to fit the CCC criterion of $V_{max} \approx 1$ $Jk_B^{-1}T^{-1}$ or $V_{max} \approx 10$ $Jk_B^{-1}T^{-1}$, respectively. The determined FEBEX bentonite colloid ζ-potential (see Figure 6a) and the best fit face electrokinetic potential (see Figure 6b) as well as all estimated edge electrokinetic potentials of α-alumina, α-$alumina_{Kup}$, γ-alumina, and 5% structural Al-ratio (see Figure 7a–d) are used. The concentrations needed to reach the criterion $V_{max} \approx 1$ $Jk_B^{-1}T^{-1}$ or $V_{max} \approx 10$ $Jk_B^{-1}T^{-1}$, respectively, for each contact mode (total, EF, EE, FF) are given in the Supplementary information (see Tables S7–S10).

To reach the criterion $V_{max} \approx 1$ $Jk_B^{-1}T^{-1}$ or $V_{max} \approx 10$ $Jk_B^{-1}T^{-1}$, respectively, higher electrolyte concentrations than the Na-CCC are needed. A trend to higher electrolyte concentrations in basic pH conditions cannot be observed. The FF interaction is always repulsive and dominates the total interaction energy, and the modelled electrolyte concentrations are higher than the measured Na-CCC. These results can be explained by the following considerations:

(1) The short distance interaction energy (<5 nm) is overvalued in the DLVO model. In all calculated cases, Born repulsion and hydration forces are responsible for the colloid–colloid repulsion. (2) The agglomeration is favoured by a secondary minimum. A deflocculation of colloids with a secondary minimum of $|V_{min}| \geq$ 5–20 $Jk_B^{-1}T^{-1}$ [76–78,81,83] is not possible anymore. The model calculations always show a secondary minimum with $|V_{min}| \geq 20$ $Jk_B^{-1}T^{-1}$. A secondary minimum agglomeration can take place and the energy barrier is not overcome. (3) The geometrical estimation for the colloid edge surface area with an aspect ratio of 1:55 is higher compared to the literature date of 1:10 [41]. A higher edge surface area leads to a decrease of the influence of the FF interaction energy.

Jasmund and Lagaly [26] state that all modes of interaction are possible for clay colloids. A pre-orientation of the bentonite platelets should not be found at the used low colloid concentration of 3.7×10^{-4}–8×10^{-4}% w/w [26]. The FF interaction dominates in the alkaline pH region due to the large face surface area. The EF interaction will take place mainly in the circum-neutral pH of 6–7, since the Al edge electrokinetic potentials are positive and the surface electrokinetic potential is negative. The edge electrokinetic potential is not shielded by the overlapping basal surface electric double layer and no spillover effect can be observed for electrolyte concentrations >10–100 mmol L^{-1} [84]. For this electrolyte concentration, Chang and Sposito [85] observe no influence of the spillover effect in their theoretical calculations for the EF interaction. The measured Na-CCC values and the calculated concentrations for reaching $V_{max} \leq 1$ $Jk_B^{-1}T^{-1}$ or $V_{max} \leq 10$ $Jk_B^{-1}T^{-1}$ in the EF mode of interaction are always greater than 10–100 mmol L^{-1} (see Figure 10). An EF aggregation should therefore not be retarded by shielding of the edge surface electrokinetic potential. The calculated EF-CCC values increase with higher pH, like the measured Na-CCC (see Figure 10). In general, higher electrolyte concentrations than the Na-CCC are modelled for $V_{max} \leq 10$ $Jk_B^{-1}T^{-1}$. With the criterion $V_{max} \leq 1$ $Jk_B^{-1}T^{-1}$, EF-CCC values below the measured Na-CCC values are observed for pH 8 and 9.

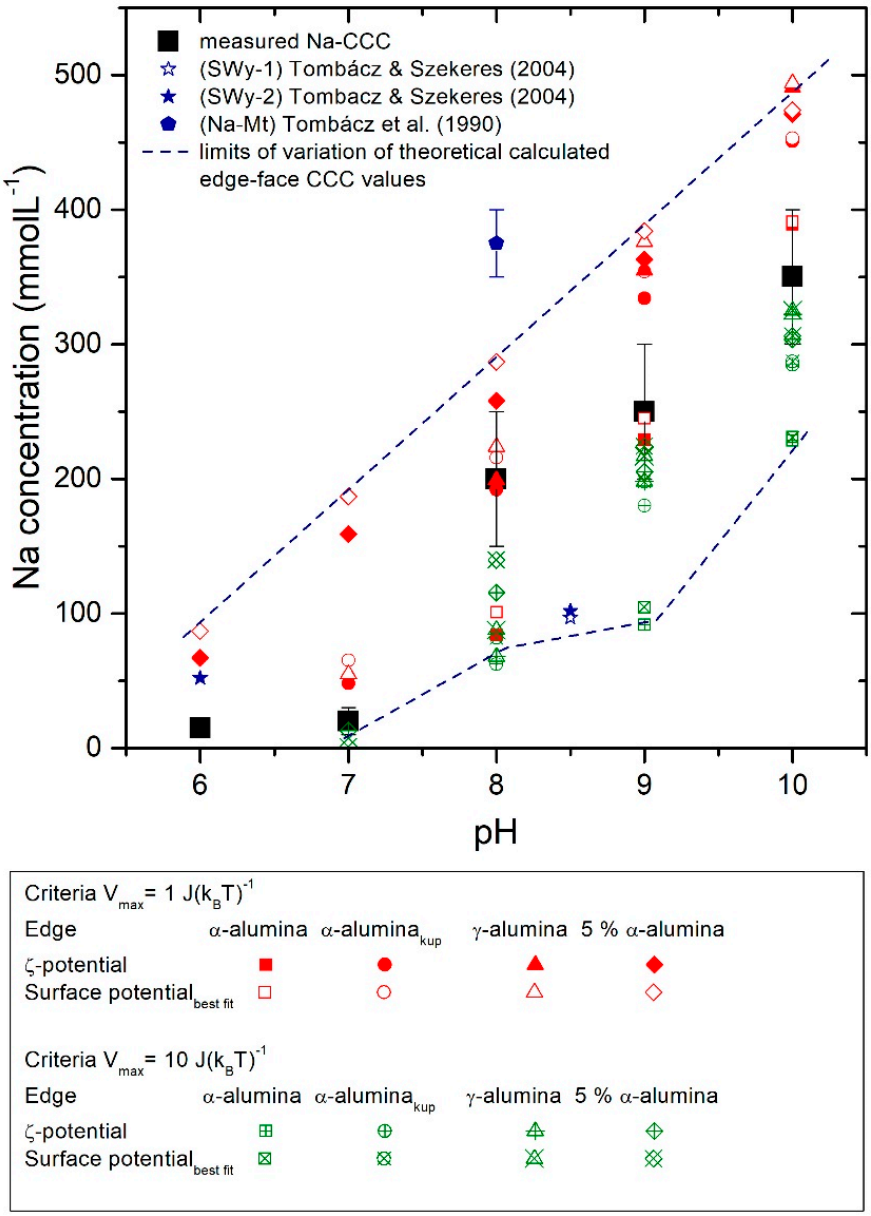

Figure 10. Concentrations fitted with the DLVO model to reach the criteria $V_{max} \leq 1\ Jk_B^{-1}T^{-1}$ or $V_{max} \leq 10\ Jk_B^{-1}T^{-1}$, respectively, for the EF mode of interaction. The fitted ζ-potential of the FEBEX bentonite colloids (see Figure 6a) and the best fit surface electrokinetic potential (see Figure 6b), and the edge electrokinetic potential calculated with α-alumina (see Figure 7a), α-alumina$_{Kup}$ (see Figure 7b), γ-alumina (see Figure 7c), and 5% structural Al-ratio (see Figure 7d) are used. As comparison, the measured Na-CCC values as well as literature data from Tombácz and Szekeres [59] and Tombácz et al. [60] are given.

Charge regulation in the electrical double layer can have important implications for interparticle forces, and colloidal stability can have major consequences, especially when considering interactions between unequally charged surfaces [86]. The next step to overcoming the simplifications used in the model of this manuscript is to calculate the surface interactions based on the new developments made in recent years using the charge regulation code [42,43].

4. Conclusions

The measurements of colloid stability and the calculations of stability ratios were performed to determine the critical coagulation concentration (CCC) regarding dependence of pH and electrolyte concentration. For $CaCl_2$ background electrolyte solution, a pH-independent Ca-CCC of 1 mmol L^{-1} was found. This Ca-CCC confirms the safety function criteria of $[M^{2+}] > 1$ mmol L^{-1} for bentonite buffer systems stated by SKB [50]. NaCl electrolyte solution shows a pH-dependent Na-CCC with 15 ± 5 mmol L^{-1} at pH 6, 20 ± 5 mmol L^{-1} at pH 7, 200 ± 50 mmol L^{-1} at pH 8, 250 ± 50 mmol L^{-1} at pH 9, and 350 ± 100 mmol L^{-1} at pH 10, respectively. The Na-CCC values for pH ≤ 7 are in good agreement with published data for Swy-1 and beidellite [52]. The size dependence of the CCC can explain the high Na-CCC values for pH ≥ 8 found in this study and the scatter of literature data. Fully delaminated FEBEX bentonite-derived montmorillonite platelets show a maximum in size distribution with the size fraction of 40 nm [62]. For a particle thickness of δ_P of 1.2 nm and this colloid size, theoretical calculations by Liu et al. [61] predict a Na-CCC of 200 mmol L^{-1} in very good agreement with the experimental results obtained in this study.

The presence of humic substances can never be excluded in natural systems. For the Whiteshell Research Area, Canada, Vilks and Bachinski [87] reported an average DOC concentration of 0.5 mg L^{-1}. At the Grimsel Test Site (Switzerland), a DOC concentration of ≤ 1 mg L^{-1} was determined by Degueldre et al. [88] (0.24 mg L^{-1}) and Schäfer et al. [89] (1.2 ± 0.2 mg L^{-1}). The groundwater of the Äspö underground laboratory, Sweden, has a higher DOC content of 10–22 mg L^{-1} [90], with maximum values found by Kienzler et al. [91] in the CHEMLAB2 borehole of 42.3 mg L^{-1}. The addition of 1 mg L^{-1} DOC by fulvic acid (GoHy-573FA), simulating the natural background DOC concentration in granitic environments, increases the Ca/FA-CCC to 2 mmol L^{-1}. The surface charge is compensated by the adsorbed organic material on the surface of the colloids, as can be shown in STXM investigations presented in this study.

The determined Na-CCC and Ca-CCC values determine the concentrations in which the prepared FEBEX bentonite colloids do not coagulate. This is particularly of interest for investigations on the influence of bentonite colloids for the transport of radionuclides from the bentonite buffer material of high-level nuclear waste repositories.

The extended DLVO model approach by Mahmood et al. [34] takes the clay colloids platelet geometry and difference in edge and face electrokinetic potential into account, and it was used in this study. The calculations with the measured ζ-potentials of the bentonite (face) and an approximation for the face potential following the approach of Williams and Williams [39] show the general trend of higher colloid stability with higher pH values, but overestimate the observed colloid stability. Adjusting the montmorillonite face electrokinetic potential by a maximum of ±15.9 mV is sufficient to successfully reproduce the measured stability ratios. Having in mind that the ζ-potential does not represent the real surface electrokinetic potential needed in the DLVO calculations and the ζ-potential measurement uncertainties, the model approach does not precisely predict the measured colloid stability. However, the Na-CCC values can be reasonably predicted using solely the edge–face interaction energy calculated. The significant deviation of the model predictions from the experimentally determined CCC values using low electrolyte concentrations are explained by the spillover of the platelet face electrical double layer shielding the platelet edge electrokinetic potential.

Supplementary Materials: The following are available online at http://www.mdpi.com/2504-5377/4/2/16/s1. Chapter S1. DLVO calculations. Figure S1. XRD diffractogram of the bentonite colloids used throughout this study. Figure S2. (**a**) AFM image of a representative Febex bentonite colloid adsorbed onto a mica. (**b**) line profile over the Febex bentonite colloid indicated by the line in (**a**). The line profile is not corrected for tip artifacts. The total number of samples n = 10. Table S1. List of values used for the calculations. Table S2. Linear fit ζ-potential of the measured ζ-potential of Febex bentonite colloids in NaCl and $CaCl_2$ background electrolyte solution. Table S3. Used ζ-potential of silica (Aerosil90, Degussa) for the DLVO calculations in NaCl and $CaCl_2$ background electrolyte solution. Table S4. ζ-potential of alumina phases used in the DLVO calculations in NaCl and $CaCl_2$ background electrolyte solution. Table S5. Estimated edge electrokinetic ζ-potential for the DLVO calculations in NaCl and $CaCl_2$ background electrolyte solution. Table S6. Face surface electrokinetic ζ-potential (best fit) after fitting the W_{DLVO} values to the $W_{measured}$ values in NaCl and $CaCl_2$ background electrolyte solution.

The surface electrokinetic potentials in NaCl background electrolyte solution are the average values of all used alumina phases. The $CaCl_2$ background electrolyte solution is solely calculated with α-alumina. Table S7. Fitted theoretical CCC concentrations to match the CCC criteria of $V_{max} \leq 1\ Jk_B{}^{-1}T^{-1}$ and $V_{max} \leq 10\ Jk_B{}^{-1}T^{-1}$ using the DLVO approach with constant surface potential and estimated edge electrokinetic potential (α-alumina). Table S8. Fitted theoretical CCC concentrations to match the CCC criteria of $V_{max} \leq 1\ Jk_B{}^{-1}T^{-1}$ and $V_{max} \leq 10\ Jk_B{}^{-1}T^{-1}$ using the DLVO approach with constant surface potential and estimated edge electrokinetic potential (α-alumina taken from Kupcik et al. [71]). Table S9. Fitted theoretical CCC concentrations to match the CCC criteria of $V_{max} \leq 1\ Jk_B{}^{-1}T^{-1}$ and $V_{max} \leq 10\ Jk_B{}^{-1}T^{-1}$ using the DLVO approach with constant surface potential and estimated edge electrokinetic potential (γ-alumina taken from de Lint et al. [72]). Table S10. Fitted theoretical CCC concentrations to match the CCC criteria of $V_{max} \leq 1\ Jk_B{}^{-1}T^{-1}$ and $V_{max} \leq 10\ Jk_B{}^{-1}T^{-1}$ using the DLVO approach with constant surface potential and estimated edge electrokinetic potential for 5% structural Al-ratio (α-alumina).

Author Contributions: Conceptualisation and methodology T.S. and T.F.; software, H.S.; validation H.S., H.G., and T.S.; formal analysis, investigation, resources, data curation, H.S.; writing—original draft preparation, H.S. and T.S.; writing—review and editing, T.S., H.G., and T.F.; visualisation, H.S.; supervision, T.S.; project administration, T.S., H.G. and T.F.; funding acquisition, T.S., H.G., and T.F. All authors have read and agreed to the published version of the manuscript.

Funding: The work has received funding by the Federal Ministry of Economics and Technology (BMWi) under the joint KIT-INE, GRS research project "KOLLORADO-e" (grant agreement number 02E11203B) and "KOLLORADO-e2" (grant agreement number 02E11456A), through the Collaborative Project BELBaR (grant agreement number 295487) by the European Commission (7th Euratom Framework Programme for Nuclear Research and Training Activities; FP7/2007–2013), and through the HGF PoF-III program "NUSAFE." Furthermore, the authors would like to acknowledge the support of the CFM Project partners.

Conflicts of Interest: The authors declare no conflict of interest. The funders had no role in the design of the study; in the collection, analyses, or interpretation of data; in the writing of the manuscript, or in the decision to publish the results.

Symbols

Symbol	Entity	Name
ε_0	$C\ V^{-1}\ m^{-1}$	Dielectric permittivity of vacuum
ε_r		Relative permittivity of water at 25 °C
k	m^{-1}	Reciprocal double layer thickness
k_B	$J\ K^{-1}$	Boltzmann constant
r_H	m	Hydrodynamic radius of colloid
r		Coagulation rate
η	$N\ s\ m^{-2}$	Dynamic viscosity
T	K	Absolute temperature
μ	$m^2\ V^{-1}\ s^{-1}$	Electrophoretic mobility
ζ	V	Zeta-potential
D	$m^2\ s^{-1}$	Diffusion coefficient
C	$g\ L^{-1}$	Colloid concentration
OD		Optical density
d	m	Sample thickness
μ(E)		Mass absorption coefficient
I_0(E)		Incident flux on the sample
I(E)		Flux behind the sample
δ_P	m	Particle thickness
S_P	m^2	Particle surface area
ρ	$kg\ m^{-3}$	Density
W		Stability ratio
V	J	Interaction energy

References

1. Sellin, P.; Leupin, O.X. The use of clay as an engineered barrier in radioactive-waste management-a review. *CCM* **2013**, *61*, 477–498. [CrossRef]

2. Dohrmann, R.; Kaufhold, S.; Lundqvist, B. The Role of Clays for Safe Storage of Nuclear Waste. In *Handbook of Clay Science*; Bergaya, F., Lagaly, G., Eds.; Elsevier: Amsterdam, The Netherlands, 2013; Volume 5, pp. 677–710. [CrossRef]
3. Pusch, R. Stability of bentonite gels in crystalline rock-Physical aspects. KBS Rep. TR 83. 1983. Available online: https://www.skb.se/publikation/3102/TR83-04webb.pdf (accessed on 20 March 2020).
4. Missana, T.; Alonso, Ú.; Turrero, M.J. Generation and stability of bentonite colloids at the bentonite/granite interface of a deep geological radioactive waste repository. *J. Cont. Hydrol.* **2003**, *61*, 17–31. [CrossRef]
5. Baik, M.-H.; Cho, W.-J.; Hahn, P.-S. Erosion of bentonite particles at the interface of a compacted bentonite and a fractured granite. *Eng. Geol.* **2007**, *91*, 229–239. [CrossRef]
6. Alonso, U.; Missana, T.; Fernández, A.M.; García-Gutiérrez, M. Erosion behaviour of raw bentonites under compacted and confined conditions: Relevance of smectite content and clay/water interactions. *Appl. Geochem.* **2018**, *94*, 11–20. [CrossRef]
7. Huber, F.; Leone, D.; Trumm, M.; Moreno, L.; Neretnieks, I.; Wenka, A.; Schäfer, T. Impact of fracture geometry on bentonite erosion - a numerical study. *Appl. Clay Sci.* **2020**. (Under Review).
8. Schäfer, T.; Huber, F.; Seher, H.; Missana, T.; Alonso, U.; Kumke, M.; Eidner, S.; Claret, F.; Enzmann, F. Nanoparticles and their influence on radionuclide mobility in deep geological formations. *Appl. Geochem.* **2012**, *27*, 390–403. [CrossRef]
9. Buddemeier, R.W.; Hunt, J.R. Transport of colloidal contaminants in groundwater: radionuclide migration at the Nevada test site. *Appl. Geochem.* **1988**, *3*, 535–548. [CrossRef]
10. Kersting, A.B.; Efurd, D.W.; Finnegan, D.L.; Rokop, D.J.; Smith, D.K.; Thompson, J.L. Migration of plutonium in ground water at the Nevada Test Site. *Nature* **1999**, *397*, 56–59. [CrossRef]
11. Vilks, P.; Miller, H.G.; Doern, D.C. Natural colloids and suspended particles in the Whiteshell Research Area, Manitoba, Canada, and their potential effect on radiocolloid formation. *Appl. Geochem.* **1991**, *6*, 565–574. [CrossRef]
12. Möri, A.; Alexander, W.R.; Geckeis, H.; Hauser, W.; Schäfer, T.; Eikenberg, J.; Fierz, T.; Degueldre, C.; Missana, T. The colloid and radionuclide retardation experiment at the Grimsel Test Site: influence of bentonite colloids on radionuclide migration in a fractured rock. *Colloids Surf. A* **2003**, *217*, 33–47. [CrossRef]
13. Geckeis, H.; Schäfer, T.; Hauser, W.; Rabung, T.; Missana, T.; Degueldre, C.; Möri, A.; Eikenberg, J.; Fierz, T.; Alexander, W.R. Results of the Colloid and Radionuclide Retention experiment (CRR) at the Grimsel Test Site (GTS), Switzerland -Impact of reaction kinetics and speciation on radionuclide migration. *Radiochim. Acta* **2004**, *92*, 765–774. [CrossRef]
14. Huber, F.; Noseck, U.; Schäfer, T. *Colloid/nanoparticle Formation and Mobility in the Context of Deep Geological Nuclear Waste Disposal. Project KOLLORADO-2*; Final Report; KIT Scientific Publishing: Karlsruhe, Germany, 2014. [CrossRef]
15. Quinto, F.; Golser, R.; Lagos, M.; Plaschke, M.; Schäfer, T.; Steier, P.; Geckeis, H. Accelerator Mass Spectrometry of Actinides in Ground- and Seawater: An Innovative Method Allowing for the Simultaneous Analysis of U, Np, Pu, Am, and Cm Isotopes below ppq Levels. *Anal. Chem.* **2015**, *87*, 5766–5773. [CrossRef] [PubMed]
16. Quinto, F.; Blechschmidt, I.; Garcia Perez, C.; Geckeis, H.; Geyer, F.; Golser, R.; Huber, F.; Lagos, M.; Lanyon, B.; Plaschke, M.; et al. Multiactinide Analysis with Accelerator Mass Spectrometry for Ultratrace Determination in Small Samples: Application to an in Situ Radionuclide Tracer Test within the Colloid Formation and Migration Experiment at the Grimsel Test Site (Switzerland). *Anal. Chem.* **2017**, *89*, 7182–7189. [CrossRef]
17. Kretzschmar, R.; Holthoff, H.; Sticher, H. Influence of pH and Humic Acid on Coagulation Kinetics of Kaolinite: A Dynamic Light Scattering Study. *J. Coll. Interf. Sci.* **1998**, *202*, 95–103. [CrossRef]
18. Missana, T.; Adell, A. On the Applicability of DLVO Theory to the Prediction of Clay Colloids Stability. *J. Coll. Interf. Sci.* **2000**, *230*, 150–156. [CrossRef] [PubMed]
19. Norrfors, K.K.; Bouby, M.; Heck, S.; Finck, N.; Marsac, R.; Schäfer, T.; Geckeis, H.; Wold, S. Montmorillonite colloids: I. Characterization and stability of dispersions with different size fractions. *Appl. Clay Sci.* **2015**, *114*, 179–189. [CrossRef]
20. Novich, B.E.; Ring, T.A. Colloid Stability of Clays Using Photon Correlation Spectroscopy. *CCM* **1984**, *32*, 400–407. [CrossRef]
21. Mayordomo, N.; Degueldre, C.; Alonso, U.; Missana, T. Size distribution of FEBEX bentonite colloids upon fast disaggregation in low-ionic strength water. *Clay Miner.* **2016**, *51*, 213–222. [CrossRef]

22. Missana, T.; Alonso, U.; Fernández, A.M.; García-Gutiérrez, M. Analysis of the stability behaviour of colloids obtained from different smectite clays. *Appl. Geochem.* **2018**, *92*, 180–187. [CrossRef]
23. Villar, M.V.; Martín, P.L.; Pelayo, M.; Ruiz, B.; Rivas, P.; Alonso, E.; Lloret, A.; Pintado, X.; Gens, A.; Linares, J.; et al. *FEBEX Bentonite: Origin, Properties and Fabrication of Blocks*; ENRESA: Madrid, Spain, 1998.
24. Lanyon, G.W.; Gaus, I. Grimsel Test Site Investigation Phase VI: Main outcomes and review of the FEBEX In Situ Test (GTS) and Mock-up after 15 years of operation, NAGRA technical report NTB 15-04, NAGRA: Wettingen, Switzerland. 2016. Available online: https://www.nagra.ch/data/documents/database/dokumente/$default/Default%20Folder/Publikationen/NTBs%202014%20-%202015/e_ntb15-04.pdf (accessed on 20 March 2020).
25. Van Olphen, H. *Clay Colloid Chemistry-For. Clay Technologists, Geologists and Soil Scientists*, 2nd ed.; John Wiley & Sons: New York, NY, USA, 1977.
26. Jasmund, K.; Lagaly, G. *Tonminerale und Tone: Struktur, Eigenschaften, Anwendungen und Einsatz in Industrie und Umwelt*; Steinkopf: Darmstadt, Germany, 1993.
27. Meunier, A. *Clays*; Springer: Berlin, Germany, 2005; p. 472.
28. Kaufhold, S.; Dohrmann, R. The variable charge of dioctahedral smectites. *J. Coll. Interf. Sci.* **2013**, *390*, 225–233. [CrossRef]
29. Christidis, G.E.; Blum, A.E.; Eberl, D.D. Influence of layer charge and charge distribution of smectites on the flow behaviour and swelling of bentonites. *Appl. Clay Sci.* **2006**, *34*, 125–138. [CrossRef]
30. Sun, L.; Ling, C.Y.; Lavikainen, L.P.; Hirvi, J.T.; Kasa, S.; Pakkanen, T.A. Influence of layer charge and charge location on the swelling pressure of dioctahedral smectites. *Chem. Phys.* **2016**, *473*, 40–45. [CrossRef]
31. Missana, T.; Alonso, U.; Fernández, A.M.; García-Gutiérrez, M. Colloid properties of different smectite clays: significance for bentonite barrier erosion and radionuclide transport in radioactive waste repositories. *Appl. Geochem.* **2018**, *97*, 157–166. [CrossRef]
32. Derjaguin, B.V.; Landau, L. Theory of the stability of strongly charged lyophobicsols and the adhesion of strongly charged particles in solutions of electrolytes. *Acta Phys. URSS* **1941**, *14*, 633–662.
33. Verwey, E.J.W.; Overbeek, J.T.G. *Theory of the stability of lyophobic colloids*; Elsevier: New York, NY, USA, 1948.
34. Mahmood, T.; Amirtharajah, A.; Sturm, T.W.; Dennett, K.E. A micromechanics approach for attachment and detachment of asymmetric colloidal particles. *Colloids Surf. A* **2001**, *177*, 99–110. [CrossRef]
35. Derjaguin, B. Untersuchungen über die Reibung und Adhäsion, IV. *Colloid Polym. Sci.* **1934**, *69*, 155–164. [CrossRef]
36. Churaev, N.V.; Derjaguin, B.V. Inclusion of structural forces in the theory of stability of colloids and films. *J. Coll. Interf. Sci.* **1985**, *103*, 542–553. [CrossRef]
37. Gregory, J. Approximate expressions for retarded van der Waals interaction. *J. Coll. Interf. Sci.* **1981**, *83*, 138–145. [CrossRef]
38. Helmy, A.K.; Ferreiro, E.A. Flocculation of NH_4-montmorillonite by electrolytes. *J. Electroanal. Chem.* **1974**, *57*, 103–112. [CrossRef]
39. Williams, D.J.A.; Williams, K.P. Electrophoresis and zeta potential of kaolinite. *J. Coll. Interf. Sci.* **1978**, *65*, 79–87. [CrossRef]
40. Cama, J.; Ganor, J.; Ayora, C.; Lasaga, C.A. Smectite dissolution kinetics at 80 °C and pH 8.8. *Geochim. Et Cosmochim. Acta* **2000**, *64*, 2701–2717. [CrossRef]
41. Plaschke, M.; Schäfer, T.; Bundschuh, T.; Ngo Manh, T.; Knopp, R.; Geckeis, H.; Kim, J.I. Size Characterization of Bentonite Colloids by Different Methods. *Anal. Chem.* **2001**, *73*, 4338–4347. [CrossRef]
42. Kumar, N.; Andersson, M.P.; van den Ende, D.; Mugele, F.; Siretanu, I. Probing the Surface Charge on the Basal Planes of Kaolinite Particles with High-Resolution Atomic Force Microscopy. *Langmuir* **2017**, *33*, 14226–14237. [CrossRef]
43. Liu, J.; Sandaklie-Nikolova, L.; Wang, X.; Miller, J.D. Surface force measurements at kaolinite edge surfaces using atomic force microscopy. *J. Coll. Interf. Sci.* **2014**, *420*, 35–40. [CrossRef]
44. Artinger, R.; Buckau, G.; Geyer, S.; Fritz, P.; Wolf, M.; Kim, J.I. Characterization of groundwater humic substances: influence of sedimentary organic carbon. *Appl. Geochem.* **2000**, *15*, 97–116. [CrossRef]
45. Jacobsen, C.; Williams, S.; Anderson, E.; Browne, M.T.; Buckley, C.J.; Kern, D.; Kirz, J.; Rivers, M.; Zhang, X. Diffraction-limited imaging in a scanning transmission x-ray microscope. *Opt. Commun.* **1991**, *86*, 351–364. [CrossRef]
46. Jacobsen, C.; Wirick, S.; Flynn, G.; Zimba, C. Soft X-ray spectroscopy from image sequences with sub-100 nm spatial resolution. *J. Microsc.* **2000**, *197*, 173–184. [CrossRef]

47. Hitchcock, A.P.; Mancini, D.C. Bibliography of atomic and molecular inner-shell excitation studies. *J. Electron. Spectrosc. Relat. Phenom.* **1994**, *67*, 1–132. [CrossRef]
48. Schäfer, T.; Buckau, G.; Artinger, R.; Kim, J.I.; Geyer, S.; Wolf, M.; Bleam, W.F.; Wirick, S.; Jacobsen, C. Origin and mobility of fulvic acids in the Gorleben aquifer system: implications from isotopic data and carbon/sulfur XANES. *Org. Geochem.* **2005**, *36*, 567–582. [CrossRef]
49. Schäfer, T.; Hertkorn, N.; Artinger, R.; Claret, F.; Bauer, A. Functional group analysis of natural organic colloids and clay association kinetics using C(1s) spectromicroscopy. *J. De Phys. Iv* **2003**, *104*, 409–412. [CrossRef]
50. SKB. *Long-term safety for KBS-3 repository at Forsmark and Laxmar-a first evaluation*; TR-06-09. SKB: Stockholm, Sweden, 2006. Available online: http://www.skb.com/publication/1192585/TR-06-09.pdf (accessed on 20 March 2020).
51. SKB. *Long-Term Safety for the Final Repository for Spent Nuclear Fuel at Forsmark, Main Report of the SR-Site Project*; TR-11-01; SKB: Stockholm, Sweden, 2011; Volume II, pp. 279–552. Available online: https://skb.se/upload/publications/pdf/TR-11-01_vol2.pdf (accessed on 20 March 2020).
52. Hetzel, F.; Doner, H.E. Some colloidal properties of Beidellite: comparison with low and high charge Montmorillonites. *CCM* **1993**, *41*, 453–460. [CrossRef]
53. Séquaris, J.-M. Modeling the effects of Ca^{2+} and clay-associated organic carbon on the stability of colloids from topsoils. *J. Coll. Interf. Sci.* **2010**, *343*, 408–414. [CrossRef]
54. Sellin, P.; Nyström, C.; Bailey, L.; Missana, T.; Schäfer, T.; Červinka, R.; Koskinen, K. ELBaR: Bentonite Erosion: Effects on the Long-term Performance of the Engineered Barrier and Radionuclide Transport. In Proceedings of the 8th EC Conference on the Management of Radioactive Waste Community Policy and Research on Disposal, EURADWASTE'13, Vilnius, Lithuania, 14–17 October 2013; pp. 293–300. [CrossRef]
55. Lagaly, G.; Ziesmer, S. Colloid chemistry of clay minerals: the coagulation of montmorillonite dispersions. *Adv. Colloid Interface Sci.* **2003**, *100*, 105–128. [CrossRef]
56. Chheda, P.; Grasso, D.; van Oss, C.J. Impact of ozone on stability of montmorillonite suspensions. *J. Coll. Interf. Sci.* **1992**, *153*, 226–236. [CrossRef]
57. Delavernhe, L.; Steudel, A.; Darbha, G.K.; Schäfer, T.; Schuhmann, R.; Wöll, C.; Geckeis, H.; Emmerich, K. Influence of mineralogical and morphological properties on the cation exchange behavior of dioctahedral smectites. *Colloids Surf. A* **2015**, *481*, 591–599. [CrossRef]
58. Mermut, A.R.; Lagaly, G. Baseline studies of the Clay Minerals Society Source Clays: Layer-charge determination and characteristics of those Minerals containing 2:1 Layers. *CCM* **2001**, *49*, 393–397. [CrossRef]
59. Tombácz, E.; Szekeres, M. Colloidal behavior of aqueous montmorillonite suspensions: the specific role of pH in the presence of indifferent electrolytes. *Appl. Clay Sci.* **2004**, *27*, 75–94. [CrossRef]
60. Tombácz, E.; Ábrahám, I.; Gilde, M.; Szántó, F. The pH-dependent colloidal stability of aqueous montmorillonite suspensions. *Colloids Surf.* **1990**, *49*, 71–80. [CrossRef]
61. Liu, L.; Moreno, L.; Neretnieks, I. A Novel Approach to Determine the Critical Coagulation Concentration of a Colloidal Dispersion with Plate-like Particles. *Langmuir* **2009**, *25*, 688–697. [CrossRef]
62. Bosbach, D.; Bouby, M.; Degueldre, C.; Filby, A.; Geckeis, H.; Götz, R.; Hauser, W.; Lützenkirchen, J.; Noseck, U.; Mihai, S.; et al. Colloid impact on radionuclide migration. In *Annual Report 2008*; Geckeis, H., Klenze, R., Eds.; Research Center Karlsruhe-Institute for Nuclear Wates Disposal (INE): Karlsruhe, Germany, 2009.
63. Schäfer, T.; Chanudet, V.; Claret, F.; Filella, M. Spectromicroscopy Mapping of Colloidal/Particulate Organic Matter in Lake Brienz, Switzerland. *Environ. Sci. Technol.* **2007**, *41*, 7864–7869. [CrossRef]
64. Schäfer, T.; Michel, P.; Claret, F.; Beetz, T.; Wirick, S.; Jacobsen, C. Radiation sensitivity of natural organic matter: Clay mineral association effects in the Callovo-Oxfordian argillite. *J. Electron. Spectrosc. Relat. Phenom.* **2009**, *170*, 49–56. [CrossRef]
65. Naber, A.; Plaschke, M.; Rothe, J.; Hofmann, H.; Fanghänel, T. Scanning transmission X-ray and laser scanning luminescence microscopy of the carboxyl group and Eu(III) distribution in humic acid aggregates. *J. Electron. Spectrosc. Relat. Phenom.* **2006**, *153*, 71–74. [CrossRef]
66. Christl, I.; Kretzschmar, R. C-1s NEXAFS Spectroscopy Reveals Chemical Fractionation of Humic Acid by Cation-Induced Coagulation. *Environ. Sci. Technol.* **2007**, *41*, 1915–1920. [CrossRef]
67. Claret, F.; Schäfer, T.; Brevet, J.; Reiller, P.E. Fractionation of Suwannee River Fulvic Acid and Aldrich Humic Acid on alpha-Al_2O_3: Spectroscopic Evidence. *Environ. Sci. Technol.* **2008**, *42*, 8809–8815. [CrossRef]
68. Stöhr, J. *NEXAFS Spectroscopy*; Springer: Berlin, Germany, 1996; Volume 25, p. 403.

69. Dhez, O.; Ade, H.; Urquhart, S.G. Calibrated NEXAFS spectra of some common polymers. *J. Electron. Spectrosc. Relat. Phenom.* **2003**, *128*, 85–96. [CrossRef]
70. Francis, J.T.; Hitchcock, A.P. Inner-shell spectroscopy of p-benzoquinone, hydroquinone, and phenol: distinguishing quinoid and benzenoid structures. *J. Phys. Chem.* **1992**, *96*, 6598–6610. [CrossRef]
71. Kupcik, T.; Rabung, T.; Lützenkirchen, J.; Finck, N.; Geckeis, H.; Fanghänel, T. Macroscopic and spectroscopic investigations on Eu(III) and Cm(III) sorption onto bayerite (β-$Al(OH)_3$) and corundum (α-Al_2O_3). *J. Coll. Interf. Sci.* **2016**, *461*, 215–224. [CrossRef]
72. de Lint, W.B.S.; Benes, N.E.; Lyklema, J.; Bouwmeester, H.J.M.; van der Linde, A.J.; Wessling, M. Ion Adsorption Parameters Determined from Zeta Potential and Titration Data for a gamma-Alumina Nanofiltration Membrane. *Langmuir* **2003**, *19*, 5861–5868. [CrossRef]
73. Franks, G.V.; Gan, Y. Charging behavior at the Alumina-Water interface and implications for ceramic processing. *J. Am. Ceram. Soc.* **2007**, *90*, 3373–3388. [CrossRef]
74. Kosmulski, M. pH-dependent surface charging and points of zero charge II. Update. *J. Coll. Interf. Sci.* **2004**, *275*, 214–224. [CrossRef] [PubMed]
75. Missana, T.; Alonso, Ú.; García-Gutiérrez, M.; Mingarro, M. Role of bentonite colloids on europium and plutonium migration in a granite fracture. *Appl. Geochem.* **2008**, *23*, 1484–1497. [CrossRef]
76. Lewis, J.A. Colloidal Processing of Ceramics. *J. Am. Ceram. Soc.* **2000**, *83*, 2341–2359. [CrossRef]
77. Marmur, A. A kinetic theory approach to primary and secondary minimum coagulations and their combination. *J. Coll. Interf. Sci.* **1979**, *72*, 41–48. [CrossRef]
78. Molina-Bolívar, J.A.; Galisteo-González, F.; Hidalgo-Álvarez, R. Repeptization Determined by Turbidity and Photon Correlation Spectroscopy Measurements: Particle Size Effects. *J. Coll. Interf. Sci.* **1997**, *195*, 289–298. [CrossRef]
79. Bagchi, P. Test for particle size dependence in the theory of slow flocculation at a secondary minimum. *Colloid Polym. Sci.* **1976**, *254*, 890–894. [CrossRef]
80. Van de Ven, T.G.M. *Colloid Hydrodynamics*; Academic Press: London, UK, 1989.
81. Litton, G.M.; Olson, T.M. Particle size effects on colloid deposition kinetics: evidence of secondary minimum deposition. *Colloids Surf. A* **1996**, *107*, 273–283. [CrossRef]
82. Wan, J.; Tokunaga, T.K.; Saiz, E.; Larsen, J.T.; Zheng, Z.; Couture, R.A. Colloid Formation at Waste Plume Fronts. *Environ. Sci. Technol.* **2004**, *38*, 6066–6073. [CrossRef]
83. Hogg, R.; Yang, K.C. Secondary coagulation. *J. Coll. Interf. Sci.* **1976**, *56*, 573–576. [CrossRef]
84. Secor, R.B.; Radke, C.J. Spillover of the diffuse double layer on montmorillonite particles. *J. Coll. Interf. Sci.* **1985**, *103*, 237–244. [CrossRef]
85. Chang, F.-R.C.; Sposito, G. The Electrical Double Layer of a Disk-Shaped Clay Mineral Particle: Effects of Electrolyte Properties and Surface Charge Density. *J. Coll. Interf. Sci.* **1996**, *178*, 555–564. [CrossRef]
86. Trefalt, G.; Behrens, S.H.; Borkovec, M. Charge Regulation in the Electrical Double Layer: Ion Adsorption and Surface Interactions. *Langmuir* **2016**, *32*, 380–400. [CrossRef]
87. Vilks, P.; Bachinski, D.B. Characterization of organics in whiteshell research area groundwater and the implications for radionuclide transport. *Appl. Geochem.* **1996**, *11*, 387–402. [CrossRef]
88. Degueldre, C.; Pfeiffer, H.R.; Alexander, W.; Wernli, B.; Bruetsch, R. Colloid properties in granitic groundwater systems. I: Sampling and characterisation. *Appl. Geochem.* **1996**, *11*, 677–685. [CrossRef]
89. Schäfer, T.; Geckeis, H.; Bouby, M.; Fanghänel, T. U, Th, Eu and colloid mobility in a granite fracture under near-natural flow conditions. *Radiochim. Acta* **2004**, *92*, 731–737. [CrossRef]
90. Tullborg, E.-L.; Gustafsson, E. 14C in bicarbonate and dissolved organics—a useful tracer? *Appl. Geochem.* **1999**, *14*, 927–938. [CrossRef]
91. Kienzler, B.; Vejmelka, P.; Römer, J.; Fanghänel, E.; Jansson, M.; Eriksen, T.E.; Wikberg, P. Swedish-German actinide migration experiment at ÄSPÖ hard rock laboratory. *J. Cont. Hydrol.* **2003**, *61*, 219–233. [CrossRef]